Fundamental Research 5 (2025) 1047–1062

Contents lists available at ScienceDirect

Fundamental Research

journal homepage: http://www.keaipublishing.com/en/journals/fundamental-research/

Article

# Engineered in-situ-forming biomimetic hydrogel with self-regulated immunostimulatory capacity promotes postoperative tumor treatment

Zhuo Cheng[a,1], Yan Hu[b,1], Yingqi Liu[a], Xuan Wang[a], Rui Xue[a], Kaiyong Cai[b], Liqi Li[c,*], Menghuan Li[a,*], Zhong Luo[a,d,*]

[a] School of Life Science, Chongqing University, Chongqing 400044, China
[b] Key Laboratory of Biorheological Science and Technology, Ministry of Education, The National "111" Project for Biomechanics and Tissue Repair Engineering, Chongqing University, Chongqing 400044, China
[c] Department of General Surgery, Xinqiao Hospital, Army Medical University, Chongqing 400037, China
[d] 111 Project Laboratory of Biomechanics and Tissue Repair, College of Bioengineering, Chongqing University, Chongqing 400044, China

ARTICLE INFO

*Article history:*
Received 14 September 2022
Received in revised form 18 December 2022
Accepted 2 February 2023
Available online 2 June 2023

*Keywords:*
Injectable in-situ forming hydrogel
Cooperative ferroptosis-immunotherapy
Microenvironment remodeling
Postoperative tumor therapy
Supramolecular bioresponsive prodrug

ABSTRACT

Post-resection tumors with microscopic foci and immunosuppressive microenvironments have high risk of recurrence and metastasis but respond poorly to various therapies. Herein, we propose a biomimetic hydrogel as a biocompatible, biodegradable and bioadhesive postoperative dressing that could be formed in situ by $NaIO_4$-initiated thiourea-catechol crosslinking after syringe-injection into the resection cavity. The thiourea or catechol-bearing hyaluronic acid precursors are also separately engineered with phenylboronic acid and $\beta$-cyclodextrin ($\beta$-CD) groups, potentiating the reversible immobilization of (1S, 3R) RAS-selective lethal 3 (RSL3) and glycosylated granulocyte macrophage-colony stimulating factor (GM-CSF) without invasive chemical reactions. Meanwhile, the interconnected porous superstructure of the hydrogels allows the incorporation and self-regulated delivery of PD-L1 antibody (aPD-L1). RSL3-induced immunogenic ferroptosis and GM-CSF could cooperatively trigger robust adaptive tumor-specific immune responses, while aPD-L1 further alleviates the accumulated immunoresistance of tumor cells due to interferon $\gamma$-mediated PD-L1 upregulation, thus stimulating potent local and whole-body antitumor immunity to prevent postoperative tumor recurrence and metastasis. The biomimetic hydrogel may serve as a promising solution for the postoperative treatment of solid tumors.

## 1. Introduction

Surgical resection is a mainstream treatment against solid tumors, but the prevention of postoperative tumor recurrence is still challenging due to various detrimental factors including microscopic residual tumors and surgical stress-induced immune dysfunction [1–4]. Adjuvant localized chemotherapy or radiotherapy is often necessary after the resection of primary tumors, which could continuously inhibit tumor growth post-resection and improve patient survival with reduced systemic toxicity [5,6]. Interestingly, these adjuvant therapies could induce immunogenic cell death (ICD) and sensitize remaining tumor cells to immune cell-mediated cytotoxic activities [7,8], thus offering potential antitumor synergy with immunotherapy to present highly specific cytotoxic action, systemic immune response, and long-term immunological memory against selected tumor cell types, all of which are highly promising for preventing local recurrence and distal tumors after resecting the primary tumors [9,10]. Recent insights reveal that ferroptosis, a recently identified regulated cell death pathway characterized by the accumulation of lethal iron-catalyzed lipid peroxides, has intrinsic connection with T cell-mediated antitumor immunity [11–14]. On one hand, ferroptosis is a highly immunogenic cell death mode that releases abundant damage-associated molecular patterns (DAMPs) including high mobility group box 1 (HMGB1) and adenosine 5′-triphosphate (ATP), which could be sensed by pattern recognition receptors on APCs to stimulate tumor-specific adaptive immune responses [15–17]. On the other hand, interferon-$\gamma$ (IFN-$\gamma$) secreted by $CD8^+$ T cells may inhibit the SLC3A2 and SLC7A11 subunits of glutamate–cystine antiporter system xc− in tumor cells to impair glutathione (GSH) biosynthesis and amplify the ferroptotic damage [18,19]. Consequently, the rational combination of ferroptosis and immunotherapy could yield potent and durable tumor inhibition efficacy for postoperative treatment.

* Corresponding authors.
*E-mail addresses:* menghuanli@cqu.edu.cn (M. Li), luozhong918@cqu.edu.cn (Z. Luo).
[1] These authors contributed equally to this work.

https://doi.org/10.1016/j.fmre.2023.02.029

Based on the previous insights regarding post-resection adjuvant therapies, in situ administration of ferroptosis inducers and immunostimulatory agents is a promising approach to concentrate their therapeutic activity while reducing systemic adverse impacts. However, surgical stress in the resected tumor bed would disrupt key immunological events including maturation of antigen-presenting cells (APCs) and development of tumor-specific $CD4^+$ and $CD8^+$ T cells, thus consolidating a highly immunosuppressive microenvironment [20,21]. Moreover, IFN-$\gamma$ would upregulate programmed death-ligand 1 (PD-L1) expression on tumor cells and potentially undermine the persistence of T cell-mediated antitumor immunity [22,23]. Remarkably, injectable in-situ forming hydrogel has attracted increasing interest for cancer therapy and tissue engineering applications and provides an effective solution for postoperative tumor treatment [24–27]. These hydrogel systems could be prepared by injecting solubilized polymeric precursors into the defected tissue and subsequently applying a physical or chemical trigger to initiate crosslinking, leading to the formation of closely-fitted hydrogels with good shape adaptability and tissue adherence for maximum coverage of residual tumor foci in the wound margin. Moreover, the hydrogels present abundant modification sites and interconnected porous superstructures for the incorporation of various functional moieties and therapeutic components, allowing facile control over their drug delivery properties [28,29]. On the basis of these insights, we hypothesize that rationally designed in situ-forming hydrogels have the potential to realize the therapeutic synergisms between ferroptosis and immunotherapy with minimal systemic side effects.

In this study, we report that the tumor surgical bed could be therapeutically modulated for cooperative ferroptosis-immunotherapy using an injectable in-situ forming biomimetic hydrogel based on bioderived constituents to prevent locoregional and systemic postoperative tumor recurrence (Fig. 1). For this purpose, we synthesized two types of functionalized hydrogel precursors by conjugating hyaluronic acid (HA), a major constituent of the extracellular matrix, with dopamine and thiourea groups, which could be syringe-delivered to the resected cavity and rapidly form closely-fitted hydrogels with high bioadhesiveness after the addition of a safe dose of $NaIO_4$ solution [30]. To exert the postoperative antitumor activities, the thiourea or dopamine-conjugated HA precursors were also separately modified with phenylboronic acid (HA-NCSN-PBA) or $\beta$-CD (HA-CD-DA) side groups, which could trap glycosylated GM-CSF and (1S, 3R) RAS-selective lethal 3 (RSL3) via boronic ester ligation and physical host-guest molecular inclusion, respectively. Furthermore, the hydrogel presents highly interconnected pores that allows the facile loading of macromolecular PD-L1 antibodies (aPD-L1). After integration into the resection cavity, the implanted hydrogels could be gradually degraded and release the therapeutic contents in-situ in a self-regulated manner. Specifically, RSL3 induces tumor cell ferroptosis that releases tumor-derived DAMPs into the surrounding microenvironment to enhance the immunogenicity of residual tumor cells, which are in turn recognized by GM-CSF-stimulated APCs to activate tumor-specific effector T cells and elicit both local and systemic antitumor immunity [31,32]. Meanwhile, the enhanced effector function of activated T cells also disrupts the glutamate uptake by residual tumor cells and amplifies their ferroptosis susceptibility via IFN-$\gamma$-SLC7A11 axis. Furthermore, the concurrently released aPD-L1 ameliorates the adaptive immune resistance in the postoperative microenvironment due to IFN-$\gamma$-mediated PD-L1 upregulation and maintains the effector function of activated T cells for durable protection against tumor recurrence post-resection [33]. In addition to the ferroptosis-immunotherapy synergism, this injectable hydrogel also enables immediate tight wound sealing and rapid recovery from the surgical injury, taking advantage of its biomimetic features including dopamine-mediated strong tissue adherence and pore-facilitated nutrient/gas exchange [34–36]. The injectable hydrogel system prevents the local tumor recurrence and distal tumors in mice bearing resected B16F10 and 4T1 tumors with negligible toxic effects, indicating its clinical potential for the postoperative care of various solid tumor indications.

## 2. Materials and methods/experiment

### 2.1. Materials

Hyaluronic acid, $\beta$-cyclodextrin, dopamine hydrochloride, 4-aminophenylboric acid, 4-toluenesulfonyl chloride, adipic acid dihydrazide, methyl isothiocyanate were supplied by Sigma-Aldrich. N-hydroxy succinimide (NHS), 1-(3-dimethylamino propyl)-3-ethyl carbodiimide hydrochloride (EDC), sodium periodate, absolute ethanol, acetone, N'N-dimethylformamide, deuterium oxide, Sulfo-Cyanine5 (Cy5) were purchased from Aladdin China. Cellular glutathione peroxidase assay kit, Annexin V-FITC apoptosis detection kit, ATP assay kit, GSH assay kit, DAPI, and TUNEL kit were purchased from Beyotime. CRT, HMGB1, and SLC7A11 were supplied by Proteintech (Wuhan, China). APC anti-CD45, APC anti-CD11c, FITC anti-CD80, PE anti-CD86, FITC anti-CD4, PE anti-CD8, PE anti-MHC II, FITC anti-IFN-$\gamma$, PE anti-F4/80 were purchased from Biolegend. Murine aPD-L1 purchased from BioXcell. Murine GM-CSF was purchased from PeproTech. Red blood cell lysis buffer was obtained from Solarbio (Beijing, China).

### 2.2. Cell lines and animal models

B16F10-luc and 4T1-luc cell lines were bought from Yeze Shanghai Biological Technology Co. LTD. C57BL/6 and BALB/c mice (female, 6-week-old) were provided by Chongqing Medical University and all mice were kept in the animal house of Chongqing Medical University. All institutional and national guidelines for the care and use of laboratory animals were followed. All characterizations were carried out following the Animal Management Rules of the Ministry of Health of the People's Republic of China. The Animal Ethics Committee of Chongqing Medical University have reviewed and approved all the experimental procedures in this study (SYXK-PLA-20120031).

### 2.3. Synthesis of $NH_2$-$\beta$-cyclodextrin

First, 31.7 mmol of $\beta$-CD was added to a 500 mL round bottom flask and dissolved in 300 mL deionized water. Meanwhile, 98.4 mmol of sodium hydroxide was dissolved in 8 mL of deionized water and added dropwise to $\beta$-CD solution within 5 minutes. 31.7 mmol of 4-toluenesulfonyl chloride was dissolved in 18 mL of acetonitrile and then added dropwise to the mixture under ice bath conditions, which was stirred continuously at room temperature for 3 hours. After the reaction, the pH was adjusted to neutral with hydrochloric acid solution. The mixed solution was recrystallized in a refrigerator under 4 °C overnight, afterwards the precipitate was collected and dispersed into acetone and ethanol solutions to remove unreacted 4-toluenesulfonyl chloride. TOS-$\beta$-CD was obtained by recrystallization, purification, and precipitation with distilled water for multiple times and the moisture was removed via vacuum freeze-drying.

The resulting TOS-$\beta$-CD (3.0 g, 2.33 mmol) was dissolved in 15 mL of anhydrous N, N-dimethylformamide. Under the protection of nitrogen, 3 mL of ethylenediamine solution was added dropwise through a syringe, and then the reaction mixture was stirred at 60 °C for 12 hours. After the reaction, the reaction solution was cooled naturally to room temperature and slowly dropped into 150 mL of acetone solution to extract the raw product via precipitation. The precipitates were recovered via filtration, washed, and precipitated again with ethanol (50 mL) and acetone (50 mL) twice. The purified precipitate was redissolved in water (2 mL) and recrystallized with ethanol and acetone (150 mL). The raw products were further dialyzed against deionized water with a dialysis bag (500Da, MWCO, Millipore) for 3 days, afterwards the moisture was removed via vacuum freeze-drying to obtain $NH_2$-$\beta$-CD. The $NH_2$-$\beta$-CD was characterized using $^1H$ NMR (400 MHz, $D_2O$, ppm) analysis.

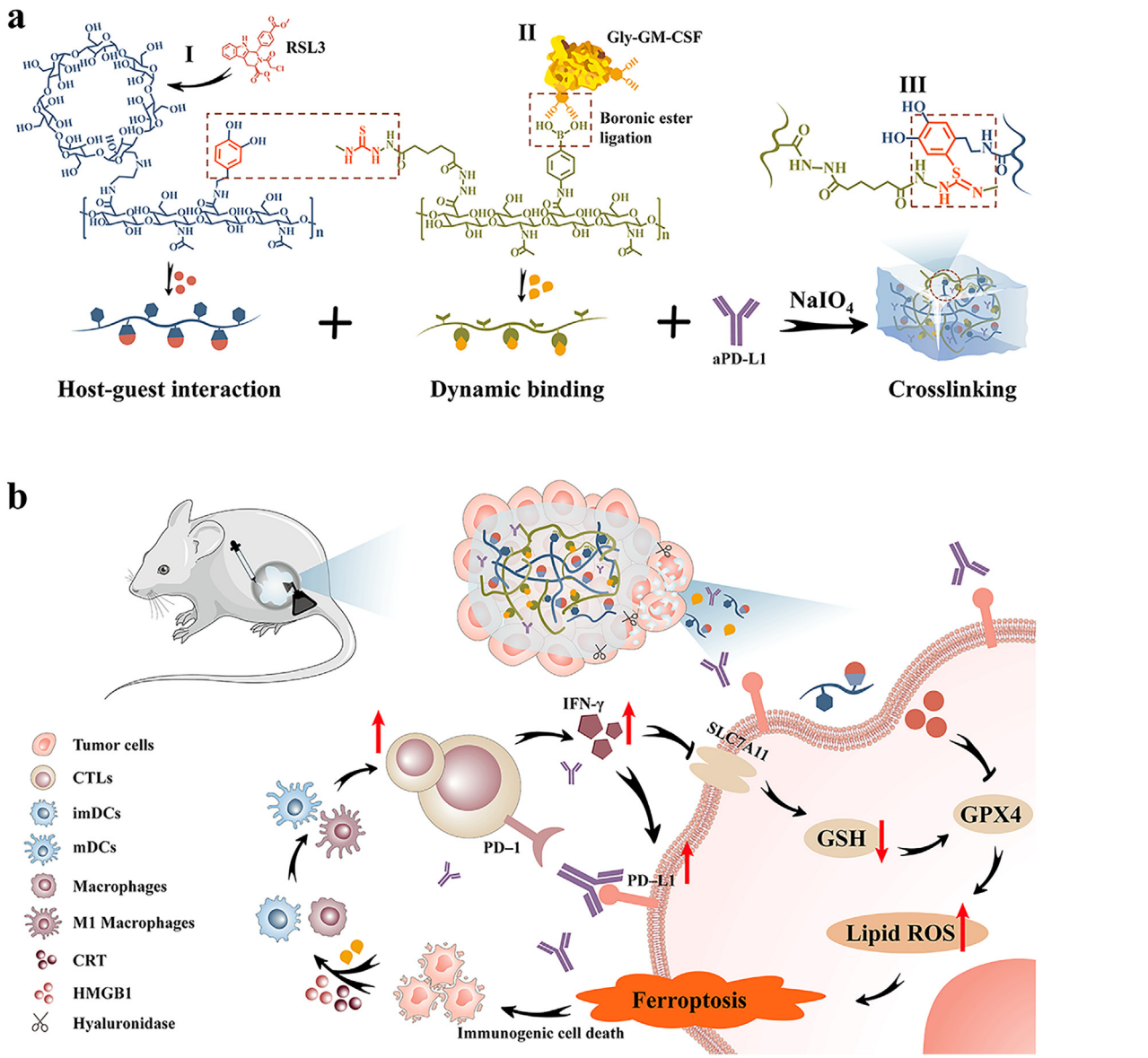


**Fig. 1. Injectable in-situ forming biomimetic hydrogel mediates cooperative ferroptosis-immunotherapy to elicit durable protection against postoperative tumor recurrence and metastasis.** (a) Molecular structures of the HA-based precursors and the gelation mechanics. (b) Schematic illustration of hydrogel-mediated cooperative ferroptosis-immunotherapy after in-situ implantation.

### *2.4. Synthesis of HA-CD and HA-CD-DA*

In 100 mL hexamethylene buffer was firstly dissolved 1 g of hyaluronic acid and then added with EDC/NHS (3.9 mmol: 3.9 mmol). The activation reaction would last 1 h under room temperature. $NH_2$-$\beta$-CD was added to the solution at a hyaluronic acid: $NH_2$-$\beta$-CD ratio of 1:1.5 and stirred at room temperature for 36 h. After the reaction, the solution was transferred to a dialysis bag (3000Da, MWCO, Millipore) and dialyzed against deionized water for 72 h. The water was changed every 4 hours. Afterwards, the solution was freeze-dried to obtain HA-CD and characterized by $^1$H NMR (400 MHz, $D_2O$, ppm).

In 50 mL of MES buffer was dissolved 500 mg HA-CD and added with EDC / NHS (2.1 mmol: 2.1 mmol), which was further incubated at room temperature for 1 h to activate the carboxyl groups. Dopamine hydrochloride (DA) was added at a hyaluronic acid: dopamine hydrochloride ratio of 1:1.5. The reaction mixture was stirred under $N_2$ protection at room temperature for 24 hours, afterwards it was transferred to a dialysis bag (500Da, MWCO, Millipore) and dialyzed against deionized water first at pH 6 for 24 h and then under neutral pH for 48 h. The water medium was changed every 4 h and the reaction solution was eventually freeze-dried to obtain HA-CD-DA. The structure of the product was analyzed by $^1$H NMR (400 MHz, $D_2O$, ppm).

For the loading of RSL3, 500 mg HA-CD-DA was dissolved in 20 mL of deionized water. Meanwhile, 5 mg RSL3 was dissolved in methanol and then dropped into HA-CD-DA solution. The mixture was first stirred at room temperature for 8 h and subsequently centrifuged at 12000 rpm for 10 min. The supernatant was collected and freeze-dried to obtain HA-CD-DA@RSL3.

### *2.5. Synthesis of HA-NCSN and HA-NCSN-PBA*

1 g of hyaluronic acid was dispersed in 100 mL of deionized water and then mixed with 2.396 g of EDC, 1.914 g of HOBt and 34.84 g of adipic acid dihydrazide (ADH). The solution was stirred for 6 h with constant addition of NaOH to maintain the pH value at about 6.8, followed by dialysis first with sodium chloride for 3 days and then deion-

ized water for another 3 days. The purified solution was freeze-dried to obtain HA-ADH. To synthesize HA-NCSN, HA-ADH was dissolved in deionized water at a concentration of 1% (w/v) and added with excessive methyl isothiocyanate dissolved in dimethyl sulfoxide at a methyl isothiocyanate: HA-ADH ratio of 5:1. The mixture was further stirred in nitrogen atmosphere for 3 days and dialyzed first with sodium chloride for 3 days and then deionized water for another 3 days. The solution was freeze-dried to obtain HA-NCSN. The structure was analyzed by $^1$H NMR (400 MHz, $D_2O$, ppm).

500 mg HA-NCSN was dissolved in MES buffer and added with EDC/NHS (2.1 mmol: 2.1 mmol), followed by incubation at room temperature for 1 hour. 4-aminophenylboric acid was added at the HA-NCSN: 4-aminophenylboric acid ratio of 1:1.5, stirred at room temperature for 24 h and eventually the solution was transferred to a dialysis bag (500da, MWCO, Millipore) for dialysis against deionized water for 3 days, during which the water was changed every 4 h. Sample-containing solution was processed through freeze-drying to obtain HA-NCSN-PBA. The structure was analyzed by $^1$H NMR (400 MHz, $D_2O$, ppm).

500 mg HA-NCSN-PBA was dissolved in 50 mL of 0.2 M disodium hydrogen phosphate solution at pH 9 and added with 20 μg of GM-CSF, stirred at room temperature for 6 h and eventually freeze-dried to obtain HA-NCSN-PBA@GM-CSF.

### 2.6. Preparation of the biomimetic hydrogel

HA-CD-DA@RSL3 and HA-NCSN-PBA@GM-CSF solutions with a concentration of 30 mg/mL were mixed at the volume ratio of 1:2, followed by the addition of anti-PD-L1 antibody (aPD-L1) at 0.6 mg/mL and further stirred at 4 ˚C for 2 hours. $NaIO_4$ solution was added to the mixed solution at a $NaIO_4$/HA molar ratio of 0.03: 1 to initiate hydrogel formation.

### 2.7. Morphology and mechanical properties of hydrogel

The morphology of the hydrogel was observed by scanning electron microscopy (SEM) after freeze-drying. The rheological properties of hydrogels were determined by a rotational rheometer, and the young's modulus of hydrogels was determined on a universal tensile testing machine.

### 2.8. Hydrogel degradation behaviors

The net weight of the hydrogel samples was determined at the start of incubation ($M_0$) by vacuum freeze-drying, afterwards the hydrogels were placed in phosphate-buffered saline (PBS, pH 6.8, with or without HAase 100 IU/mL). All samples were incubated under gentle shaking at 37 ˚C. At predetermined time points, the gels were extracted and freeze-dried before weighing on a digital balance ($M_1$). Degradation rate was calculated using the formula ($M_0$ - $M_1$) / $M_0$ × 100%.

### 2.9. Drug release kinetics of hydrogels

The drug release profiles from the hydrogels were analyzed in phosphate-buffered saline (PBS, pH 6.8, with or without HAase 100 IU/mL) at 37 ˚C. The released RSL3 was analyzed by HPLC. The released GM-CSF and aPD-L1 were determined by GM-CSF and IgG total ELISA kit, respectively.

### 2.10. Cytotoxicity evaluation of hydrogels in vitro

B16F10 cells were cultured in RPMI1640 medium containing 10% fetal bovine serum (Gibco), while 4T1 cells and HUVECs were cultured in high glucose DMEM medium containing 10% fetal bovine serum. To evaluate the biocompatibility of hydrogel system, B16F10 cells, 4T1 cells, and HUVECs were inoculated in the bottom chamber of 24-well transwell plates at an initial cell density of 8 × $10^4$ /well and placed in an incubator under a constant temperature of 37 ˚C and a 5% $CO_2$ atmosphere. Meanwhile, hydrogel samples were pretreated with HAase-containing culture media for 1, 2 or 3 days. When the cell confluence reached around 50%, hydrogel soaking solution was added to the upper chamber of 24-well plates and cultured for another 24 h. After incubation, the chambers were removed and MTT reagents were added to detect cell viability after different treatment according to procedures in the user manual.

### 2.11. Hydrogel degradation behaviors in vivo

To track the degradation of the hydrogel in vivo, the HA precursors were first loaded with the therapeutic contents and then grafted with Cy5 by EDC/NHS reaction. Meanwhile, to establish the animal tumor model, 1 × $10^6$ B16F10 cells were subcutaneously injected into C57BL/6 mice. Ten days later, tumors were resected when they reached 200 $mm^3$, leaving about 5% of the tumor at the primary site. The Cy5-labeled hydrogels were created in the resection cavity and the wound was then sutured and sterilized. At predetermined time points, Cy5 fluorescence in mice was observed by a living-image system.

Alternatively, Cy5 was loaded into the biomimetic hydrogel via physical encapsulation to represent the encapsulated aPD-L1. 1 × $10^6$ B16F10 cells were injected subcutaneously into C57BL/6 mice. When the tumor reached 200 $mm^3$, the mice were divided into two groups (free Cy5, Cy5/gel) and received similar partial tumor resection. Cy5 hydrogel was established in the wound cavity, followed by suturing and sterilization. At predetermined time points, the retention of Cy5 fluorescence in mice was observed using a living-imaging system.

### 2.12. GPX4 activity assay in vitro and in vivo

Gel@RSL3 and Gel were soaked in hyaluronidase-supplemented media for 1, 3, and 5 days, while RSL3-containing cell culture media were aged for the same period and used for comparative analysis. B16F10 or 4T1 cells were incubated in 24-well plates with an initial cell density of 8 × $10^4$/well under the standard conditions mentioned above. Black control, Gel soaking solution, RSL3-containing culture medium, Gel@RSL3 soaking solution were added into individual well and the incubation would last for another 24 h. After incubation, the cells were collected and treated by cellular glutathione peroxidase assay kit (Beyotime) to determine the GPX4 activity. As for the in vivo analysis of GPX4 activity in tumor tissues, tumor tissues were extracted from individual groups (control, Gel, Gel@GM-CSF, Gel@RSL3, Gel@RSL3+GM-CSF, Gel@RSL3+GM-CSF+aPD-L1) and measured by the same assay kit according to the manufacturer's instructions.

### 2.13. Lipid ROS assay by BODIPY-C11 staining

B16F10 or 4T1 cells were inoculated into 24-well plates (8 × $10^4$/well). Control, Gel soaking solution, RSL3-containing culture medium, Gel@RSL3 soaking solution were added to individual wells for 24 h incubation. After incubation, cells were collected for staining by 5 μM BODIPY 581/591 C11 in 1 mL PBS and incubated at 37 ˚C for 30 min. The cells were washed 3 times and resuspended in 300 μL fresh PBS for flow cytometric analysis. Alternatively, B16F10 cells were seeded on confocal dishes (1 × $10^5$/well) and treated by the same procedures for CLSM imaging.

For the co-incubation system with immune cells, B16F10 and 4T1 cells were inoculated into 24-well plates (8 × $10^4$/well) under standard conditions and then treated by control, Gel soaking solution, Gel@GM-CSF soaking solution, Gel@RSL3 soaking solution, Gel@RSL3+GM-CSF soaking solution and Gel@RSL3+GM-CSF+aPD-L1 soaking solution for 24 h. Subsequently, immune cells extracted from the spleen of mice were inoculated in the 24-well plates. After incubating overnight at 37 ˚C under an atmospheric $CO_2$ level of 5%, the floating immune cells

were discarded and remaining tumor cells were analyzed with Lipid ROS assay kit to determine the lipid ROS levels.

### 2.14. Evaluation of the antitumor efficacy in vitro

B16F10 or 4T1 cells were inoculated into 24-well transwell plates ($8 \times 10^4$/well). Control, Gel soaking solution, RSL3-containing culture medium, Gel@RSL3 soaking solution were added to the upper chamber of individual wells for 24 h incubation. After incubation, cells in the bottom chambers were collected and stained with Annexin V/PI cell assay kit (Beyotime) for flow cytometric analysis.

For the co-incubation system with immune cells, B16F10 or 4T1 cells were inoculated into 24-well plates ($8 \times 10^4$/well) and then treated by control, Gel soaking solution, Gel@GM-CSF soaking solution, Gel@RSL3 soaking solution, Gel@RSL3+GM-CSF soaking solution and Gel@RSL3+GM-CSF+aPD-L1 soaking solution for 24 h. Afterwards, immune cells extracted from the spleen of mouse were co-inoculated in the bottom chamber of the 24-well plates. After incubating overnight at 37 ˚C under an atmospheric $CO_2$ level of 5%, the tumor cells were extracted for survival analysis. Same procedures have been applied for flow cytometric analysis of tumor cell survival.

### 2.15. Evaluation of immunogenic cell death of tumor cells

B16F10 or 4T1 cells were inoculated into confocal dishes ($1 \times 10^5$/dish). Control, Gel soaking solution, RSL3-containing culture medium, Gel@RSL3 soaking solution were added to individual dish for 24 h incubation. After incubation, cells were washed with PBS for 3 times, treated with CRT and HMGB1 antibodies and incubated overnight at 4 ˚C. Subsequently, fluorescent secondary antibodies were added for incubation at 37 ˚C for 2 h, followed by DAPI staining at 37 ˚C for 10 minutes. Finally, the samples were washed with PBS and observed by a Leica TCS SP8 confocal laser microscope.

For the tests on ATP release, B16F10 or 4T1 cells were inoculated into 24-well transwell plates ($8 \times 10^4$/well). Control, Gel soaking solution, RSL3-containing culture medium, Gel@RSL3 soaking solution were added to the upper chamber of individual wells for 24 h incubation. After incubation, the supernatant in the bottom chamber of different groups was collected and analyzed with ATP assay kit (Beyotime).

### 2.16. Gel@GM-CSF induces maturation of BMDCs and RAW264.7 cells

C57BL/6 mice were euthanized and sterilized by soaking in 75% ethanol for 10 minutes. After that, the femur of the mice was extracted under sterile conditions. The attached muscle tissues were carefully removed and the epiphyses on both ends of the femur were cut off. Bone marrow was extracted with a sterile 1 mL syringe and the medullary cavity was washed repeatedly. The extracted bone marrow and washing solution of medullary cavity were suspended with culture media, filtered with a 300-mesh nylon net, and centrifuged at 1200 rpm for 5 minutes. After centrifugation, the supernatant was removed and 2 mL of red blood cell lysis buffer was added to resuspend the cells. 5 mL of culture medium was added after 5 minutes and the suspension was centrifuged at 1200 rpm for 5 minutes. Immune cells extracted from bone marrow were cultured in the medium containing granulocyte-macrophage colony-stimulating factor GM-CSF (20 ng/mL) and interleukin-4 (10 ng/mL). The medium was changed every two days. BMDCs were successfully obtained after 6 days of culture. The extracted BMDCs were inoculated into the bottom chamber of 24-well transwell plates, and the soaking solutions of Control, Gel, GM-CSF and Gel@GM-CSF for 1, 3, or 5 days were added into the upper chamber for 24 h of incubation. The BMDCs were eventually collected and the expression levels of CD80 and CD86 on their surface were detected by flow cytometry.

Alternatively, RAW264.7 cells were inoculated into the bottom chamber of 24-well transwell plates; the soaking solutions of control, Gel, GM-CSF and Gel@GM-CSF for 1, 3 or 5 days were added into the upper chamber for 24 h of incubation. RAW264.7 cells were collected to analyze the treatment-induced changes in the expression of CD80 on RAW264.7 surface.

### 2.17. Analysis of hydrogel-induced immunity in vitro

C57BL/6 mice were euthanized and sterilized by soaking in 75% ethanol for 10 minutes. The spleen tissue of mice was taken out under sterile conditions. After washing 3 times by sterile PBS, the spleen was wrapped with 300 mesh nylon net, and gently grounded in a petri dish with culture medium to extract the cells. The spleen cell suspensions were collected, filtered once through a 300-mesh nylon net and centrifuged at 1200 rpm for 5 minutes. The supernatant was removed and refilled with 3 mL red blood cell lysis buffer. 5 mL culture medium was added after 5 minutes and the mixture was centrifuged at 1200 rpm for 5 minutes. The supernatant was removed and the residual cells were cultured with RPMI1640 culture medium.

B16F10 or 4T1 cells were inoculated into the bottom chamber of 24-well transwell plates at the initial cell number was $8 \times 10^4$/well, followed by the adding the soaking solutions of control, Gel, Gel@GMCSF, Gel@RSL3, Gel@RSL3+GMCSF, Gel@RSL3+GM-CSF+aPD-L1 into the upper chamber for 24 h incubation. The culture media were extracted and the splenic immune cells were added to the bottom chamber for another 24 h of incubation. The splenic immune cells were collected afterward and centrifuged at 1200 rpm for 5 minutes. $CD80^+/CD86^+$, $F4/80^+/CD80^+$, $CD4^+/CD8^+$ and $CD8a^+/IFN\text{-}\gamma^+$ ratios in different immune cell populations were detected by flow cytometry, while the culture media were used to detect the secretion levels of IFN-$\gamma$, TNF-$\alpha$ and GzmB by ELISA.

### 2.18. Treatment-induced expression of PD-L1 in tumor cells

B16F10 or 4T1 cells were inoculated into the bottom chamber of 24-well transwell plates at the initial cell number of $8 \times 10^4$/well under standard conditions, followed by adding the soaking solutions of control, Gel, Gel@GMCSF, Gel@RSL3, Gel@RSL3+GMCSF, Gel@RSL3+GM-CSF+aPD-L1 to the upper chamber for 24 h incubation. The culture media were removed and the splenic immune cells were added to the bottom chamber for another 24 h of incubation. After the co-culture, the tumor cells were collected and centrifuged at 1200 rpm for 5 minutes. APC anti-PD-L1 was used to detect the PD-L1 expression of tumor cells by flow cytometry.

### 2.19. Treatment-induced changes in GSH levels

B16F10 or 4T1 cells were inoculated into the bottom chamber of 24-well transwell plates at the initial cell number of $8 \times 10^4$/well under standard conditions, followed by adding the soaking solutions of control, Gel, Gel@GMCSF, Gel@RSL3, Gel@RSL3+GMCSF, Gel@RSL3+GM-CSF+aPD-L1 to the upper chamber for 24 h incubation. The culture media were removed and the splenic immune cells were added to the bottom chamber for another 24 h of incubation. After co-culture, the tumor cells were collected and the GSH levels were detected by GSH assay kit (Beyotime).

### 2.20. Evaluation on treatment-induced changes in MDA levels

B16F10 or 4T1 cells were inoculated into the bottom chamber of 24-well transwell plates at the initial cell number of $8 \times 10^4$/well under standard conditions, followed by adding the soaking solutions of control, Gel, Gel@GMCSF, Gel@RSL3, Gel@RSL3+GMCSF, Gel@RSL3+GM-CSF+aPD-L1 to the upper chamber for 24 h incubation. The culture media were removed and the splenic immune cells were added to the bottom chamber for another 24 h of incubation. After co-culture, the tumor cells were collected and the cellular MDA levels were detected by MDA assay kit (Beyotime). The MDA levels in tumor tissues were measured by the same assay kit.

### 2.21. Western blot analysis

B16F10 or 4T1 cells were inoculated into a 6-well plate and co-cultured with the soaking solutions of control, Gel, Gel@GMCSF, Gel@RSL3, Gel@RSL3+GMCSF, and Gel@RSL3+GM-CSF+aPD-L1 for 24 hours. Afterwards, the tumor cells were collected and the total protein was determined by BCA protein assay kit. Protein immunoassay was performed by SDS-PAGE electrophoresis and finally photographed by a molecular imaging apparatus (Versa doc MP 4000 system, Bio-Rad). The expression levels of CRT, HMGB1 and SLC7A11 were observed and analyzed using $\beta$-Actin as the internal standard.

### 2.22. Hydrogel-induced antitumor immunity in vivo

42 female C57BL/6 mice were purchased and housed in Chongqing Medical University with an average age of around 4-6 weeks and weight of around 18 g. All animal tests have been reviewed and approved by the Animal Care and Use Committee of Laboratory Animals Administration of Chongqing Medical University and followed the national and institutional guidelines. Each mouse was injected with PBS solution containing $1 \times 10^6$ B16F10-luc cells to establish the tumor animal model. When the tumor volume grew to about 200 $mm^3$, the mice were randomly divided into 6 groups with 7 mice in each group (Control, Gel, Gel@GMCSF, Gel@RSL3, Gel@RSL3+GMCSF, and Gel@RSL3+GM-CSF+aPD-L1). Body weight and tumor volumes of each group were maintained at the same level. The mice were anesthetized by intraperitoneally injecting 100 μL of 4% chloral hydrate solution. Tumors were partially resected that around 5% of the original tumors remained in the primary site. 150 μL of HA precursor solutions (3%) were injected into the wound cavity, followed by spraying sodium periodate solution (0.05%) to initiate in situ gelling. Finally, the hydrogel-filled wounds were sutured and sterilized. The dimensions of the tumors were measured using a digital calliper once every three days and the tumor volume was calculated using the formula $V_{tumor} = L \times W^2/2$ (L: longitudinal diameter of the tumor, W: cross-sectional diameter of the tumor). After 21 days of treatment, the mice were euthanized, and tumor and main organs were excised and washed with PBS 3 times. Subsequently, the major organs and tumors were embedded into paraffin sections and then stained with H&E and TUNEL kit. Immune cells were extracted from the tumors by fluorescence-activated cell sorting using various fluorescently labelled antibodies including FITC anti-CD80, PE anti-CD86, APC anti-CD3, FITC anti-CD4, PE anti-CD8, PE anti-F4/80, APC anti-CD11c, APC anti-CD45 for flow cytometric analysis. For determining the intratumoral infiltration of T cells, tumors were dissected and sliced into thin sections after formaldehyde fixation, treated using 50 μL of PE anti-CD4 and PE anti-CD8, and incubated in a 4-degree refrigerator for 8h. Finally, the infiltration of immune cells in tumor tissue was observed on a fluorescence confocal microscope. The secretion levels of IFN-$\gamma$, TNF-$\alpha$ and GzmB in serum were analyzed by ELISA.

### 2.23. Survival analysis

B16F10-luc tumor-bearing mice were randomly divided into 6 groups with 7 each (Control, Gel, Gel@GMCSF, Gel@RSL3, Gel@RSL3+GMCSF, and Gel@RSL3+GM-CSF+aPD-L1). The number of live mice in each group was recorded once every 3 days until day 60.

### 2.24. Construction of bilateral tumor model and treatment

The B16F10 tumor-bearing C57BL/6 mice were constructed by subcutaneously injecting $1\times10^6$ B16F10-luc cells into the right flank of C57BL/6 mice. After 7 days, $1 \times 10^6$ B16F10-luc cells were injected to the left flank to establish the secondary tumors. When the right tumor grew to 200$mm^3$, mice were randomly divided into 6 groups with 7 mice each (Control, Gel, Gel@GM-CSF, Gel@RSL3, Gel@RSL3+GM-CSF, Gel@RSL3+GM-CSF+aPD-L1). The mice were anesthetized by intraperitoneally injecting 100 μL of 4% chloral hydrate solution. Tumors were partially resected that around 5% of the original tumors remained in the primary site. 150 μL of HA precursor solutions (3%) were injected into the wound cavity, followed by spraying sodium periodate solution (0.05%) to initiate in situ gelling. Finally, the hydrogel-filled wounds were sutured and sterilized. The tumor size, weight, and survival rate of mice during treatment were recorded. After 21 days of treatment, the mice were euthanized, and the left tumors of the mice were extracted and washed with PBS. The infiltration of immune cells in the left tumor and the maturation of DC cells in lymph nodes were analysed by flow cytometry.

### 2.25. Statistical analysis

All data were processed in GraphPad Prism (version 8.0 for Windows) by Student's t-test. * indicates significance at $P < 0.05$, ** indicates significance at $P < 0.01$, *** indicates significance at $P < 0.001$, **** indicates significance at $P < 0.0001$.

## 3. Results and discussion

### 3.1. Synthesis of the polymeric precursors and their gelation properties

The HA-CD-DA and HA-NCSN-PBA precursors were firstly synthesized using well-established reaction routes. Specifically, HA-CD-DA was obtained by the procedural conjugation of aminated $\beta$-CD and dopamine via EDC/NHS coupling. The substitution degree of $\beta$-CD and dopamine on the HA backbone was around 19% and 24%, respectively. Based on similar conjugation mechanisms, aminated PBA and NCSN moieties were sequentially accommodated on HA at a substitution degree of 22% and 33% to afford HA-NCSN-PBA. The resultant products were thoroughly characterized using $^1$H NMR (Fig. S1), which not only validated their chemical composition but also confirmed that the desired biopolymeric precursors were successfully synthesized with high yield and purity. Due to the conjugation of abundant $\beta$-CD and PBA moieties on HA-CD-DA and HA-NCSN-PBA precursors, they could not only efficiently trap RSL3 and glycosylated GM-CSF molecules via reversible host-guest inclusion and boronic ester ligation for localized drug delivery, but also avoid additional invasive chemical modification on these therapeutic agents to retain their in vivo activity. Adding small amounts of $NaIO_4$ solution into the mixture of HA-CD-DA and HA-NCSN-PBA caused almost instant gel formation, and the underlying mechanism is that the catechol groups in dopamine would be first oxidized by $NaIO_4$ into quinones and then react with the thiourea groups in the NCSN moieties through the highly efficient thiourea-quinone coupling reaction, during which the quinone groups were reduced to catechol moieties [37]. In contrast, the gelation of pristine HA-CD-DA via oligomerization of $NaIO_4$-oxidized catechol groups took more than 30 min (Fig. 2a, b). SEM imaging of the obtained hydrogel samples revealed a highly interconnected porous structure, which potentiates the facile delivery of aPD-L1 and is also beneficial for removing wound exudate and facilitating nutrient/gas transport to the wound area to accelerate wound healing (Fig. 2c) [38,39]. Importantly, comparative rheological analysis showed that HA-CD-DA/HA-NCSN-PBA hydrogel has much higher bioadhesiveness than HA-CD-DA-only counterparts, ascribing to the NCSN-mediated reduction of quinone to catechol groups to maintain the tissue-adhering capacity of dopamine units [40]. Typically, Fig. 2d showed that the HA-CD-DA/HA-NCSN-PBA hydrogel could reliably adhere to various tissues and organs including heart, liver, spleen, lung, kidney and B16F10/4T1 tumors, suggesting its potential application in a lot of clinically relevant scenarios. Mechanical analysis of the hydrogel samples prepared at graded HA-CD-DA/HA-NCSN-PBA feeding ratios (w/w) not only confirmed the successful gel formation but also revealed that the storage modulus (G') was the greatest under the HA-CD-DA/HA-NCSN-PBA feeding ratio of 1:2, which was used as the standard set-up for the subsequent experiment. Quantitative HPLC and ELISA tests on the hydro-

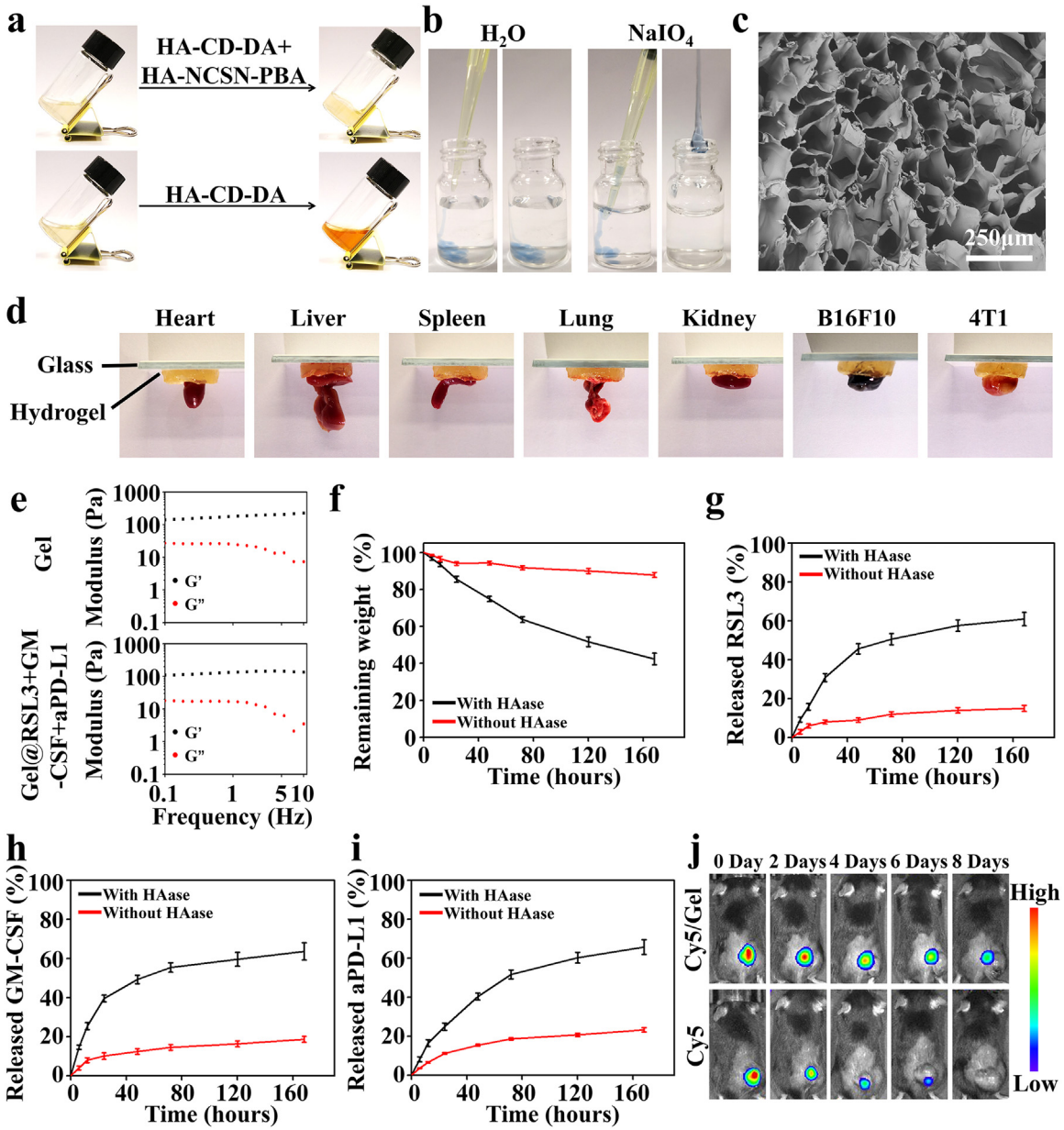


**Fig. 2. The HA-based biomimetic hydrogel demonstrates fast gelation rate, biomimetic mechanical properties, controlled drug release kinetics and biodegradability.** (a) Gelation behaviors of HA-CD-DA and HA-NCSN-PBA precursors. (b) Photographical illustration of the $NaIO_4$-initiated rapid gelation in aqueous environment. The mixture solution of the HA precursors was directly injected into $NaIO_4$ solution (w/v 0.05%). (c) SEM image of the hydrogels after freeze-drying. (d) Adhesion behavior of hydrogel on various organs and tissues. (e) Comparative analysis on the mechanical properties of the hydrogel with or without drug loading. (f) Degradation profiles of hydrogel with or without hyaluronidase treatment. (g-i) Release kinetics of RSL3, GM-CSF and aPD-L1 from the hydrogel with or without HAase stimulation. (j) In vivo fluorescence images showing the degradation and drug release properties of the hydrogel after implantation.

gel samples revealed that the loading ratios of RSL3, GM-CSF and aPD-L1 under standard conditions were 2%, 0.02% and 2.2%, respectively. Moreover, the high loading ratios of therapeutic components induced only negligible changes in the mechanical performance of the hydrogel system (Figs. 2e and S2).

HA is a naturally occurring polysaccharide universally present in the connective tissues of human body and could be degraded by hyaluronidase in a time-dependent manner, which consolidates the mechanistic basis for the self-regulated and sustained release of the therapeutic cargos in the resected tumor bed for enduring protection [41]. To investigate the hyaluronidase-mediated degradation of the HA-based hydrogels, samples were processed in PBS buffer supplemented with 100 IU/mL of hyaluronidase. For ease of understanding, the HA-CD-DA/HA-NCSN-PBA composite hydrogel prepared under standard conditions was denoted as “Gel” in the following discussions. The residual Gel weight decreased steadily over time that only around 40% of the hydrogel remained after 7 days of incubation. In contrast, hydrogel weight loss was almost negligible when hyaluronidase was absent, supporting the enzyme-mediated biodegradability of the hydrogel system after implantation (Fig. 2f). Meanwhile, the release patterns of RSL3, GM-CSF and aPD-L1 were measured using HPLC and ELISA tests and were consistent with the hydrogel degradation profiles, of which the relative release ratios were 61%, 63% and 66% after 7 days of incubation (Fig. 2g-i). The release features were further evaluated on mice bearing excisional wounds, for which the HA molecules were conjugated with Cy5 for in vivo fluorescence tracking. Interestingly, the Cy5 fluorescence dropped

to an undetectable level after 16 days of incubation, indicating the complete degradation of the implanted hydrogels (Fig. S3). Alternatively, quantitative on-site drug retention test with Cy5-encapsulating Gel samples showed that around 35% of the Cy5 has been retained in the implantation site after 8 days of incubation, while Cy5 signals in mice injected with Cy5 solutions was almost negligible (Fig. 2j). The observations on hydrogel degradation and drug release collectively substantiated our hypothesis that the therapeutic cargos could be released into the surrounding tissues in a self-regulated manner over a sufficiently long period through the on-demand enzyme-mediated degradation of the HA substrate in situ, which is demonstrably advantageous over locally injected free drugs.

### 3.2. Hydrogel induces immunogenic ferroptosis of tumor cells

Before monitoring the response of tumor cells to the HA-based hydrogel system, we first investigated its cytotoxic impact against various cell lines including B16F10, 4T1 and non-malignant human umbilical vein endothelial cells (HUVECs) via MTT assay and observed no significant changes in cell viability throughout the 3-day incubation period, which was ascribed to the intrinsic biocompatibility of HA molecules and excluded the potential contribution of the hydrogel scaffold in the subsequent therapeutic evaluations (Fig. S4). We subsequently studied the ferroptosis-inducing capability of the HA-based hydrogel against tumor cells using a transwell incubation system (Fig. 3a). Here the hydrogels were first immersed in hyaluronidase-supplemented culture media for 1, 3 or 5 days (denoted as Gel@RSL3-D1, Gel@RSL3-D3 and Gel@RSL3-D5) and then transferred to the upper chamber, while tumor cells were inoculated in the bottom chamber. RSL3 solutions were aged using a similar set-up (RSL3-D1, RSL3-D3 and RSL3-D5) for comparative analysis. According to the assay results with cellular glutathione peroxidase assay kit, GPX4 activity of the Gel group remained at base line level but changed significantly in the RSL3 and Gel@RSL3 group, which could be explained by the GPX4 inhibition capability of RSL3 while again suggesting the non-toxicity of the hydrogel scaffold [42]. Interestingly, the GPX4 inhibition effect of RSL3 gradually diminished under prolonged aging. In contrast, the GPX4 inhibition effect of Gel@RSL3 showed a positive correlation with the hyaluronidase pre-activation time, for which the GPX4 activity in the Gel@RSL3-D5 was 33% lower than the control group (Figs. 3b and S5). The opposing trends between RSL3 and Gel@RSL3-mediated GPX4 inhibition confirmed that our hydrogel system protected RSL3 from various deterioration cues in the biological environment to improve the ferroptosis-mediated antitumor effect. Consistent with the variations in GPX4 activity, the lipid peroxidation level in Gel@RSL3-D5 group was 2-fold higher than that by RSL3-D5 (Figs. 3c-e and S6-7) and correlated with a tumor cell killing ratio of around 35% (Figs. 3f and S8).

It is well established that ferroptotic cells can release abundant DAMPs and are considered more immunogenic than apoptotic cells, which could be exploited for activating specialized APCs to stimulate the downstream antitumor immune effects [43]. Here the impact of the hydrogel treatment on tumor immunogenicity was investigated by monitoring the changes in typical immunostimulatory DAMPs including calreticulin (CRT), HMGB1 and ATP. ATP abundance of extracellular fluid in the Gel@RSL3-D5 group was 3.6-fold and 2.2-fold higher than that in the control and RSL-D5 group (Figs. 3g and S9). Meanwhile, western blot results in Fig. 4k showed that the expression level of membrane CRT in the Gel@RSL3-D5 group was significantly upregulated compared to the control group and RSL3-D5 (Figs. 3h-i and S10). The intracellular abundance of HMGB1 in B16F10 cells of the Gel@RSL3-D5 group has decreased substantially due to the loss of cellular contents after ferroptotic tumor cell death. Meanwhlie, HMGB1 levels in the supernatant of the Gel@RSL3-D5 group have increased by 72% (B16F10) and 70% (4T1) compared to the corresponding control groups, suggesting the significant treatment-induced enhancement in its immunostimulatory potential. (Figs. 3j-k and S11-12). These observations collectively supported that the hydrogel-mediated ferroptosis treatment could efficiently induce tumor cell ferroptosis and continuously elevate the DAMP abundance in the extracellular microenvironment, thus facilitating the antigen loading into APCs.

### 3.3. Hydrogel-stimulated activation of APCs

The postoperative tumor bed is a highly complex ecological niche with an impaired immune surveillance system, necessitating the rational cooperation of immunostimulatory modalities to promote recognition and cross-presentation of tumor-derived antigens [44,45]. The pro-maturation capacity of the hydrogel on major APC types including dendritic cells and macrophages was firstly investigated using a similar experimental set-up to ferroptosis analysis. Here Gel@GM-CSF was pre-activated using hyaluronidase-supplemented culture media for 1, 3 and 5 days and then collected together with the soaking solution for the incubation of immature APCs, of which the samples were denoted as Gel@GM-CSF-D1, Gel@GM-CSF-D3 and Gel@GM-CSF-D5. Notably, treating bone marrow-derived dendritic cells (BMDCs) with the hyaluronidase-processed hydrogels increased the frequency of mature dendritic cells (DCs) ($CD80^+CD86^+$) at varying degrees, and the pro-maturation effect was positively correlated with the hyaluronidase pre-activation time. Remarkably, the frequency of mature DCs in the Gel@GM-CSF-D5 group reached around 50%, evidently supporting the hydrogel-enhanced DC maturation status (Figs. 3l and S13). Meanwhile, treating immature macrophages with the hyaluronidase-activated Gel@GM-CSF also caused enhanced expression of macrophage maturation marker CD80 in a similar manner that facilitated their polarization into the pro-inflammatory M1 phenotype, of which the frequency of M1 macrophages increased by 2-fold after the incubation with Gel@GM-CSF-D5 (Figs. 3m and S14). These observations collectively demonstrated that the hydrogels substantially promoted the maturation of APCs to facilitate the uptake, processing and presentation of tumor-derived DAMPs. Notably, the frequency of mature DCs and macrophages in the Gel@GM-CSF-D5 group was on the same level with the free GM-CSF group, suggesting that the GM-CSF component of the hydrogel system promoted APC maturation rather than the HA-based scaffold.

### 3.4. Hydrogel-mediated cooperative ferroptosis-immunotherapy against B16F10 and 4T1 cells

Next, we thoroughly studied the therapeutic response of tumor cells to the hydrogel-mediated cooperative ferroptosis-immunotherapy. Herein, tumor cells and hydrogels were separately inoculated into the bottom and upper chambers of transwell plates and incubated for 24 h to induce immunogenic ferroptosis, afterwards ex vivo harvested splenic immune cells were added into bottom chambers to mimic in vivo immunological conditions. To investigate the general applicability of this hydrogel system, we have included two types of tumor cell lines that are the commonly employed B16F10 cells as well as the poorly immunogenic 4T1 cells. In the case of treatment against B16F10 cells, Gel@GM-CSF and Gel@RSL3 only triggered modest maturation of DCs and macrophages, which could be explained by the immunostimulatory effect of GM-CSF and ferroptosis-induced release of tumor-derived DAMPs. Contrastingly, the Gel@RSL3+GM-CSF group substantially promoted the maturation of both DCs and macrophages as it significantly upregulated MHC-II expression in DCs and CD80 in macrophages, of which the frequency was 3-fold and 4-fold higher compared to the control group, confirming our hypothesis that the Gel@RSL3+GM-CSF hydrogel system could serve as a highly integrated scaffold to enhance the APC-mediated detection of B16F10-derived antigens (Figs. 4a-b and S15a-b). The hydrogel-enhanced adaptive immune responses were further investigated by monitoring the activation status of T cells in the co-incubation system of B16F10 and splenic immune cells. We observed that the frequency of $CD4^+/CD8^+$ T cells has increased significantly in

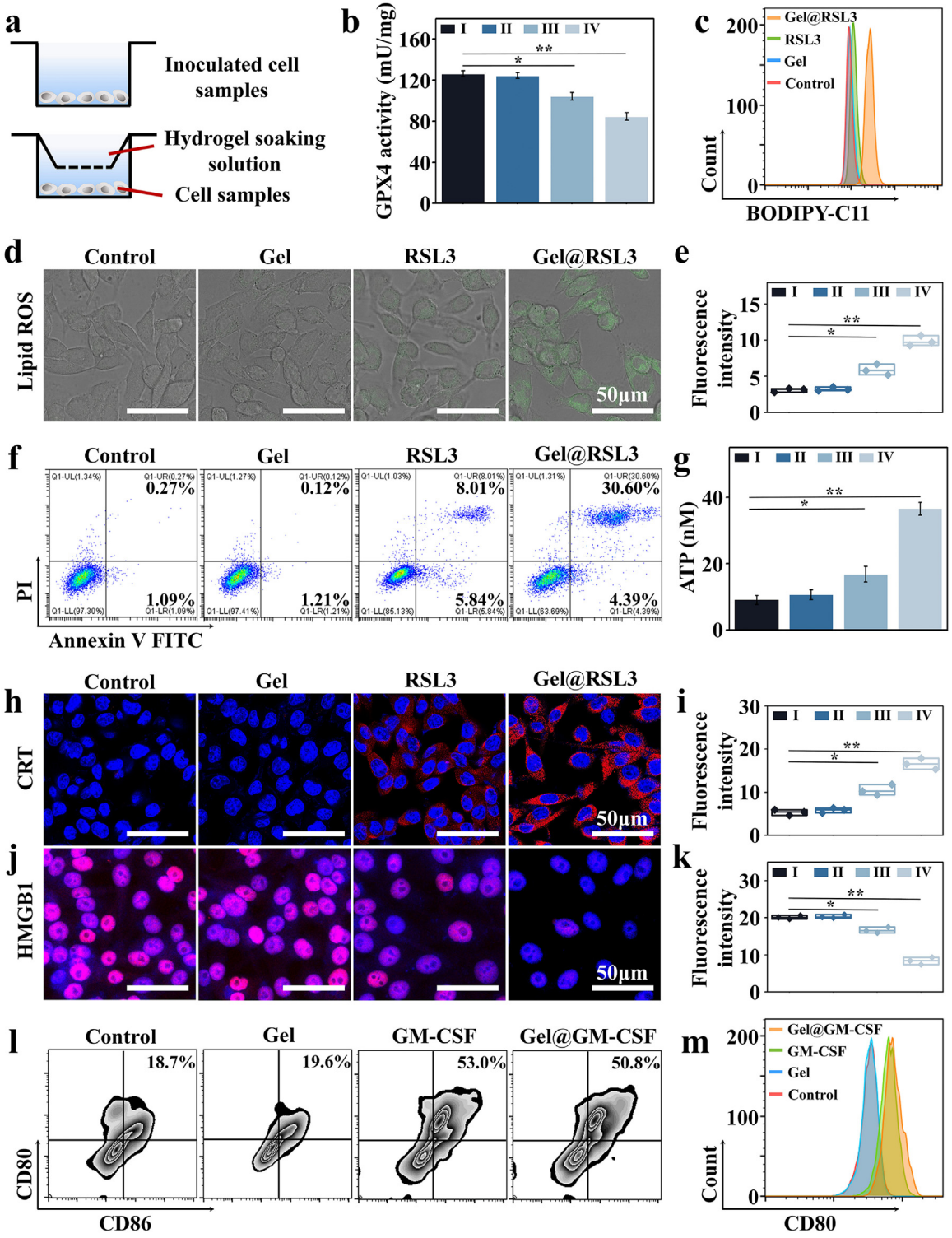


**Fig. 3. Ferroptosis-inducing and immunostimulatory capabilities of the biomimetic hydrogel.** (a) Schematic diagram for the tumor cell/immune cell co-incubation system in transwell plates. The tumor cells (B16F10, 4T1) or immune cells were inoculated in the bottom chamber of the 24-well transwell culture plate, while the hydrogel soaking solution was placed in the upper chamber. (b) Changes of GPX4 activity in B16F10 cells after different treatments. (I) Control, (II) Gel, (III) RSL3, (IV) Gel@RSL3 (n = 4). (c) Flow cytometric analysis on the lipid ROS levels in B16F10 cells after different treatments. (d) CLSM imaging of lipid ROS generation in B16F10 cells after different treatments. Higher green fluorescence intensity indicates greater lipid ROS production. (e) Quantitative fluorescence analysis of lipid ROS levels in panel D (n = 4). (f) Flow cytometric analysis on the hydrogel-mediated ferroptosis levels of B16F10 cells after different treatments. (g) ATP levels in the supernatants of cell culture after different treatments. (I) Control, (II) Gel, (III) RSL3, (IV) Gel@RSL3 (n = 4). (h) CLSM imaging of CRT expression in B16F10 cells after different treatments. Stronger red fluorescence indicates higher expression levels. (i) Quantitative fluorescence analysis of CRT expression levels in panel H (n = 4). (j) CLSM imaging of cellular HMGB1 abundance after different treatments. Lower red fluorescence indicates greater HMGB1 release into the extracellular compartment. (k) Quantitative fluorescence analysis of HMGB1 release in panel J (n = 4). (l) Flow cytometric analysis on the treatment-induced maturation of BMDCs. (m) Flow cytometric analysis on the activation status of macrophages by monitoring the CD80 expression levels. * indicates significance at $P < 0.05$, ** indicates significance at $P < 0.01$.

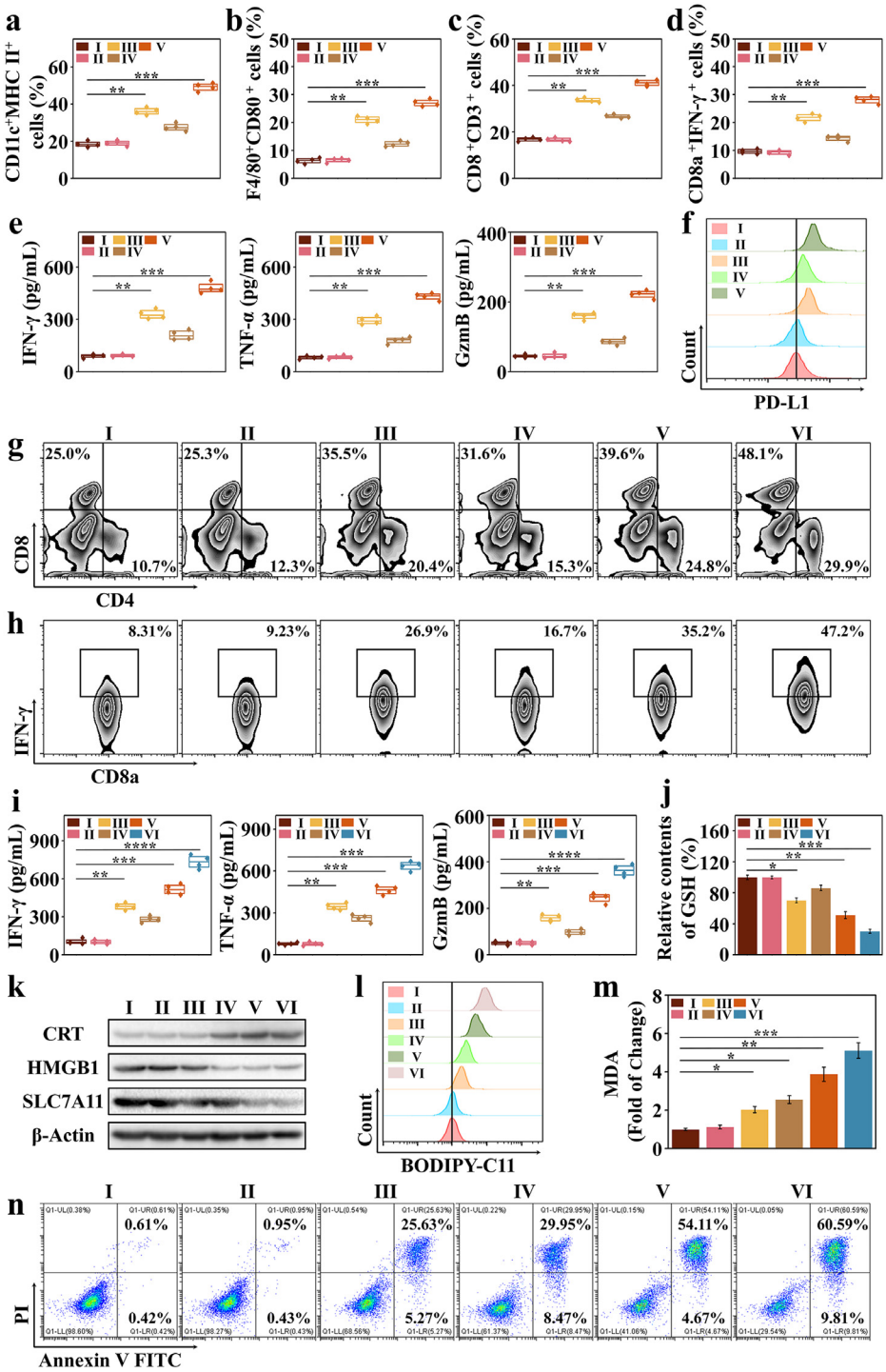


**Fig. 4. Gel@RSL3+GM-CSF+aPD-L1 activates immune response in vitro.** (a-d) Flow cytometric analysis of the activation status of DCs ($CD11c^+$/MHC $II^+$), M1 macrophages ($F4/80^+$/$CD80^+$) and T cells ($CD8^+$/$CD3^+$ and $CD8a^+$/IFN-$\gamma^+$) in the co-incubation system of splenic immune cells and B16F10 cells after treatment with (I) Control, (II) Gel, (III) Gel@GM-CSF, (IV) Gel@RSL3 and (V) Gel@RSL3+GM-CSF (n = 4). (e) Secretion levels of immunostimulatory cytokines including IFN-$\gamma$, TNF-$\alpha$ and antitumor effector molecule GzmB in the supernatant from the co-culture system after different treatments (n = 4). (f) PD-L1 expression in tumor cells with after the hydrogel-mediated ferroptosis-immunotherapy. Group set-up for panel e-f: (I) Control, (II) Gel, (III) Gel@GM-CSF, (IV) Gel@RSL3 and (V) Gel@RSL3+GM-CSF). (g-h) Flow cytometric analysis of the expression levels of effector T cell marker $CD4^+$/$CD8^+$ and $CD8a^+$/IFN-$\gamma^+$ in T cells co-incubated with B16F10 cells after treatment with (I) Control, (II) Gel, (III) Gel@GM-CSF, (IV) Gel@RSL3, (V) Gel@RSL3+GM-CSF and (VI) Gel@RSL3+GM-CSF+aPD-L1. (i) Secretion levels of immunostimulatory cytokines including IFN-$\gamma$, TNF-$\alpha$ and antitumor effector molecule GzmB in the supernatant from the co-culture system after different treatments (n = 4). (j) Evaluation on the GSH levels in B16F10 cells after different treatments (n = 4). (k) Western blot analysis of the expression level of CRT, HMGB1 and SLC7A11 in different groups. (l) Flow cytometric analysis on the lipid ROS levels in B16F10 cells after different treatments. (m) MDA levels in B16F10 cells after different treatments (n = 4). Group set-up for panel I-M: (I) Control, (II) Gel, (III) Gel@GM-CSF, (IV) Gel@RSL3, (V) Gel@RSL3+GM-CSF and (VI) Gel@RSL3+GM-CSF+aPD-L1). (n) Flow cytometric analysis on the death rate of B16F10 cells after different treatments, including (I) Control, (II) Gel, (III) Gel@GM-CSF, (IV) Gel@RSL3, (V) Gel@RSL3+GM-CSF and (VI) Gel@RSL3+GM-CSF+aPD-L1. * indicates significance at $P < 0.05$, ** indicates significance at $P < 0.01$, *** indicates significance at $P < 0.001$, **** indicates significance at $P < 0.0001$.

the Gel@RSL3+GM-CSF group by around 34% compared to the control group, accompanied with a substantial increase in their antitumor effector functions. Specifically, the IFN-$\gamma$ level in $CD8^+$ T cells of the Gel@RSL3+GM-CSF group increased by around 20%, while the IFN-$\gamma$, TNF-$\alpha$ and granzyme b (GzmB) levels in the culture media increased by 5-fold, 5.5-fold and 4.8-fold, respectively (Figs. 4c-e and S15c-d). Importantly, it is well established that IFN-$\gamma$ would induce PD-L1 upregulation in tumor cells that may enhance the risk of tumor immune escape. Consistent with the observations in previous studies [46], we detected that PD-L1 expression on tumor cells in the Gel@RSL3+GM-CSF group was 2-fold higher than the control group (Fig. 4f). Interestingly, Gel@RSL3+GM-CSF+aPD-L1 group showed significantly higher frequency of $CD4^+/CD8^+$ T cells, pro-inflammatory cytokine secretion (TNF-$\alpha$ and IFN-$\gamma$) and GzmB production than the Gel@RSL3+GM-CSF group, validating the rationale that the incorporated aPD-L1 could reduce the adaptive immune resistance of tumor cells via blocking the upregulated PD-L1 immune checkpoint on tumor cell surface (Fig. 4g-i). Furthermore, the impact of the enhanced IFN-$\gamma$ secretion on ferroptosis susceptibility of B16F10 cells was also investigated based on its SLC7A11 regulatory capability. The SLC7A11 expression and intracellular GSH abundance have both dropped substantially by 80% and 69% after the combined treatment of Gel@RSL3+GM-CSF+aPD-L1 inoculation and co-incubation with immune cells (Figs. 4j-k and S16). Due to the IFN-$\gamma$-mediated blockade of system Xc-/GSH/GPX4 axis, tumor cells in the Gel@RSL3+GM-CSF+aPD-L1 group showed significantly enhanced susceptibility to RSL3-induced ferroptosis, evidenced by the increasing levels of typical ferroptosis markers including lipoperoxides (7-fold) and MDA (5-fold) compared to control group (Fig. 4l-m). Taking advantage of the therapeutic cooperation between ferroptosis and T cell-mediated antitumor immunity, the Gel@RSL3+GM-CSF+aPD-L1 group showed superior tumor inhibition effect than the other groups with a survival rate below 30% for B16F10 cells in the co-incubation system (Fig. 4n). In addition to the evaluation on B16F10 cells, we also investigated the inhibition effect of the hydrogel on poorly immunogenic 4T1 triple-negative breast cancer cells and the results were highly consistent, supporting its therapeutic activity against a broad spectrum of solid tumor indications (Figs. S17-18).

### *3.5. Hydrogel-enabled prevention of postoperative B16F10 and 4T1 tumor recurrence in vivo*

To test the therapeutic effect of the biomimetic hydrogel in clinically relevant scenarios, it was employed as the wound dressing for partially resected B16F10-luc and 4T1-luc tumor mouse models. We observed rapid and homogenous hydrogel formation even under a low $NaIO_4$ dosage (0.03 mmol $NaIO_4$ for 1 mmol of HA precursors) with a gelation time less than 5 s, which enabled the stable dressing of the excision wound (Fig. 5b). The residual B16F10 tumors in mice implanted with blank gels showed rapid regrowth like the control group, of which the tumor volume reached around 1200$mm^3$ after 21 days of incubation. Treatment with Gel@GM-CSF and Gel@RSL3 caused modest inhibition on the growth of the residual B16F10 tumors, of which the final size at day 21 was around 800 $mm^3$ and 700 $mm^3$, ascribing to the limited antitumor efficacy of RSL3-induced ferroptosis and GM-CSF-mediated APC maturation when acting separately. The Gel@RSL3+GM-CSF+aPD-L1 group showed the most pronounced tumor inhibition effect with almost no significant changes in tumor volume throughout the 21-day treatment period (Fig. 5c, d). In line with its potent tumor inhibition effect, the Gel@RSL3+GM-CSF+aPD-L1 group showed the largest dead cell population according to H&E and TUNEL staining assay (Fig. 5j) and also significantly prolonged the survival time of the tumor-bearing mice that around 60% of the Gel@RSL3+GM-CSF+aPD-L1-implanted mice survived for at least 60 days (Fig. 5e). Notably, the hydrogels firmly adhered to the surgical tumor bed during the whole postoperative treatment session, confirming the favorable bioadhesiveness of the hydrogel system.

To elucidate the molecular mechanism underlying the superior antitumor efficacy of Gel@RSL3+GM-CSF+aPD-L1 in vivo, we further extracted the tumor tissues from the surgical site for comprehensive analyses. Treatment with RSL3-containing hydrogels (Gel@RSL3, Gel@RSL3+GM-CSF, Gel@RSL3+GM-CSF+aPD-L1) caused a significant loss of GPX4 activity in tumor cells that was in line with the GPX4-deactivating function of RSL3. Meanwhile, tumors treated by Gel-GM-CSF also revealed a moderate decrease in GPX4 activity, which could be explained by the SLC7A11/GSH/GPX4 regulatory capability of IFN-$\gamma$ secreted by activated T cells. Gel@RSL3+GM-CSF+aPD-L1 treatment induced the greatest decrease in GPX4 activity by more than 67%, suggesting that the biomimetic hydrogel system enables the synergistic integration of GPX4-inhibition functions of RSL3 and T cell-mediated immunotherapy to amplify the ferroptosis inducing efficiency (Fig. 5g). In line with the observations above, the Gel@RSL3+GM-CSF+aPD-L1 group showed the highest MDA and 4-HNE levels that were 2-fold and 4-fold higher than the control group (Figs. 5i and S19) and validated the pronounced ferroptosis damage thereof. The hydrogel-enabled tumor cell ferroptosis also improved the immunoavailability of tumor-derived DAMPs in the tumor microenvironment, as western blot and immunofluorescence tests collectively confirmed the substantial upregulation of CRT (4-fold) and HMGB1 (4-fold) in the extracted tumor tissues (Figs. 5h and S20-21). Taking advantage of the ferroptosis-induced DAMP release, GM-CSF-mediated APC stimulation effect and aPD-L1-mediated immune checkpoint inhibition, Gel@RSL3+GM-CSF+aPD-L1 substantially enhanced the overall tumor immune cell infiltration ($CD45^+$) by around 20% (Fig. 6a). Specifically, the number of tumor-resident DCs and M1 macrophages have increased by 20% and 22% compared to the control group (Fig. 6b, c), accompanied with a 36% increase in the infiltration of $CD4^+/CD8^+$ T cells. The flow cytometric test results were also supported by CD4/CD8 immunofluorescence analysis, which revealed a similar trend in the abundance of CD4/CD8 T cells in the extracted tumor tissues. In line with the expanded populations of activated tumor-specific T cells, we also observed that serum levels of IFN-$\gamma$, TNF-$\alpha$ and GzmB in the Gel@RSL3+GM-CSF+aPD-L1 increased significantly compared to the blank control and Gel@RSL3+GM-CSF, suggesting its superior capability to generate enhanced adaptive antitumor immune responses in vivo (Figs. 6d-g and S22). In addition, the antitumor performance of the hydrogel was also tested on partially resected 4T1-luc tumor mouse model to test and the results were highly consistent (Figs. S23-S24). These observations validated the hydrogel-regulated therapeutic synergism among RSL3, GM-CSF and aPD-L1 in the resected tumor bed and indicated that the postoperative treatment of Gel@RSL3+GM-CSF+aPD-L1 could elicit potent and durable antitumor immunity against a broad spectrum of solid tumor indications. Moreover, hydrogel-treated mice showed only negligible body weight changes and no histopathological abnormalities in major organs (heart, liver, spleen, lungs and kidneys), which was ascribed to the high biocompatibility of the HA precursors and the localized delivery of RSL3, again validating the safety of the hydrogel system under clinically relevant conditions (Figs. 5f and S25).

### *3.6. Abscopal effect of the biomimetic hydrogel for eliminating distal tumors*

After confirming that the ability of Gel@RSL3+GM-CSF+aPD-L1 to inhibit postoperative local tumor recurrence, we further investigated whether the locoregional hydrogel treatment could elicit systemic immune responses to offer whole-body protection against residual or recurrent tumors. For this purpose, we first inoculated B16F10-luc tumor cells into the right flank of the mice to establish the primary tumor site, and $1 \times 10^6$ units of B16F10-luc tumor cells were injected into the left flank of the mice after 7 days of incubation to mimic distant tumors. The primary tumors were partially resected at day 10 after the inoculation of the distal tumors and hydrogels were implanted into the resection cavity to initiate the postoperative treatment (Fig. 7a).

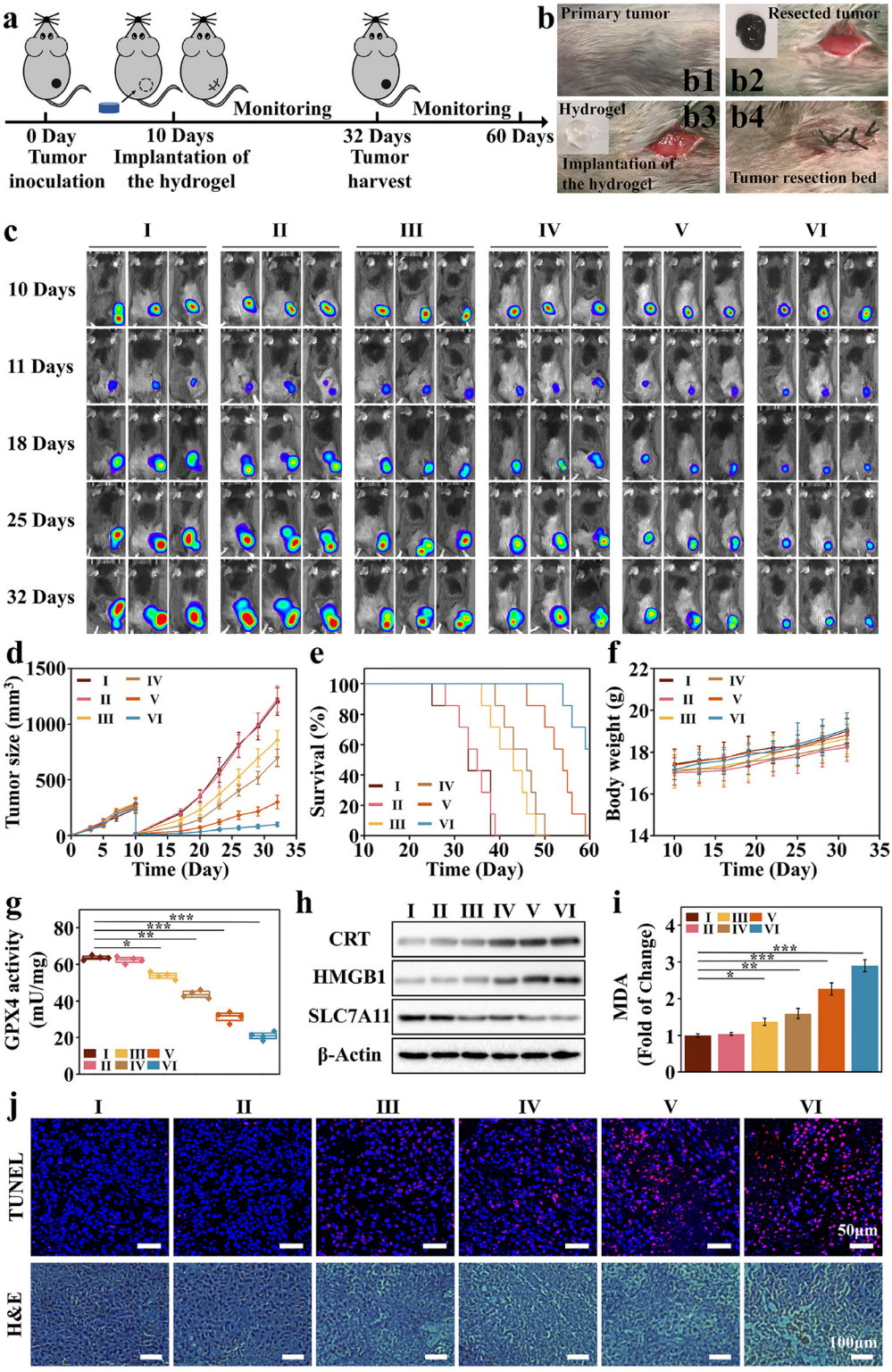


**Fig. 5. Antitumor effect of biomimetic hydrogel in vivo.** (a) Schematic illustration of the treatment scheme of the B16F10-luc tumor-bearing mice (n = 7). (b) Treatment procedures on the tumor-bearing mice. (c) In vivo bioluminescence images of B16F10-luc tumor-bearing mice throughout the treatment period with (I) Control, (II) Gel, (III) Gel@GM-CSF, (IV) Gel@RSL3, (V) Gel@RSL3+GM-CSF and (VI) Gel@RSL3+GM-CSF-aPD-L1. (d) Tumor size changes during the incubation period after different treatments. (e) Survival analysis of mice after different treatments. (f) Body weight changes after treatment with different samples. (g) Evaluation on the GPX4 activity in tumor tissues after different treatments (n = 4). (h) Western blot analysis on the expression of CRT, HMGB1 and SLC7A11 in B16F10-luc tumors after treatment with (I) Control, (II) Gel, (III) Gel@GM-CSF, (IV) Gel@RSL3, (V) Gel@RSL3+GM-CSF and (VI) Gel@RSL3+GM-CSF-aPD-L1. (i) MDA levels in tumor tissue after different treatments (n = 4). (j) H&E and TUNEL staining of tumor tissue samples after treatment (I) Control, (II) Gel, (III) Gel@GM-CSF, (IV) Gel@RSL3, (V) Gel@RSL3+GM-CSF and (VI) Gel@RSL3+GM-CSF-aPD-L1. * indicates significance at $P < 0.05$, ** indicates significance at $P < 0.01$, *** indicates significance at $P < 0.001$.

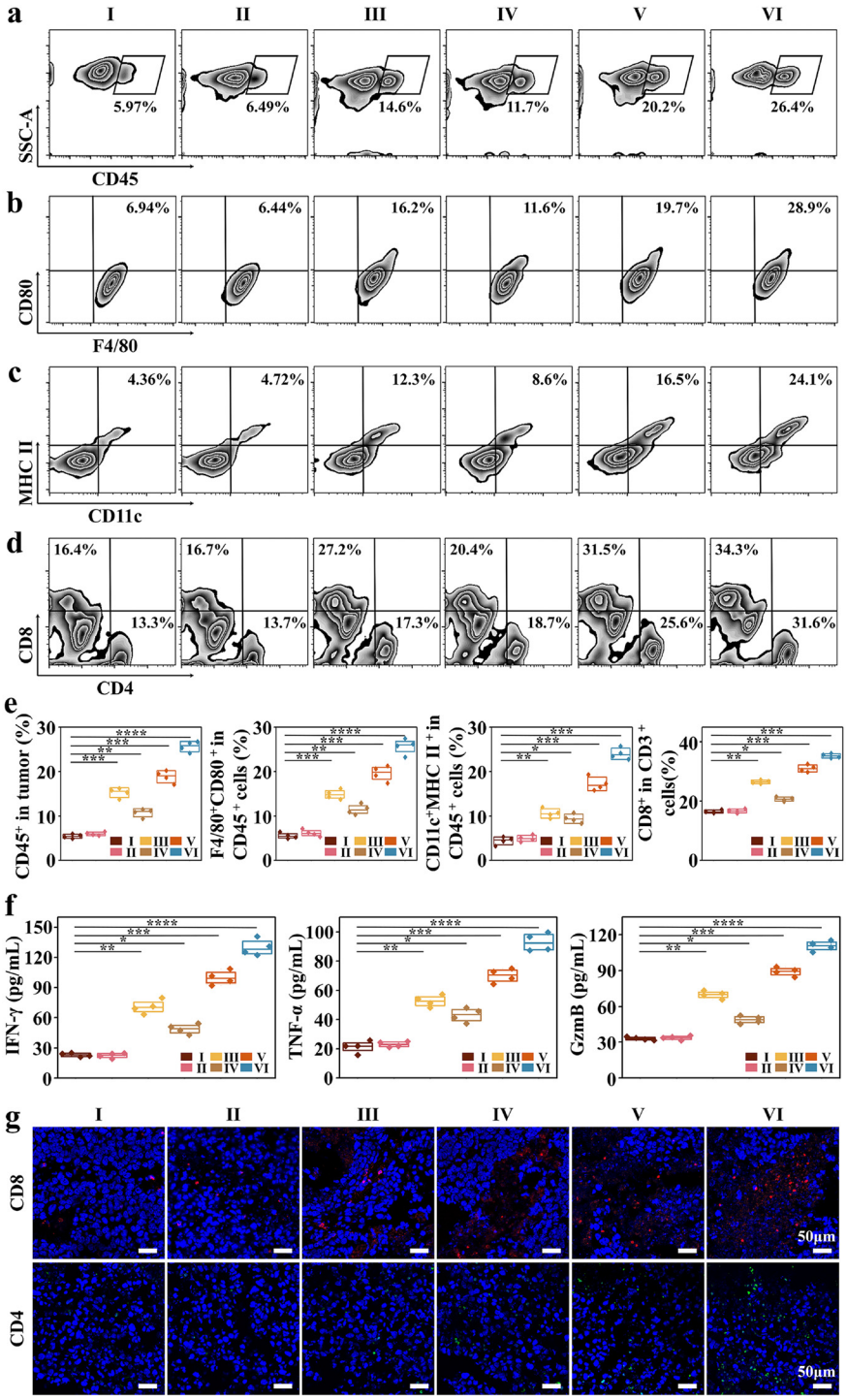


**Fig. 6. Hydrogel-mediated antitumor immune response in vivo.** (a-e) Flow cytometric analysis on the tumor infiltration of (a) total immune cells ($CD45^+$), (b) M1 macrophages ($F4/80^+/CD80^+$), (c) DCs ($CD11c^+/MHC\ II^+$) and (d) effector T cells ($CD4^+/CD8^+$) after treatment with (I) Control, (II) Gel, (III) Gel@GM-CSF, (IV) Gel@RSL3, (V) Gel@RSL3+GM-CSF and (VI) Gel@RSL3+GM-CSF-aPD-L1 in vivo (n = 4). (f) Serum levels of IFN-$\gamma$, TNF-$\alpha$ and GzmB in mice after treatment with (I) Control, (II) Gel, (III) Gel@GM-CSF, (IV) Gel@RSL3, (V) Gel@RSL3+GM-CSF and (VI) Gel@RSL3+GM-CSF-aPD-L1 (n = 4). (g) Immunofluorescence images of extracted tumors showing $CD4^+/CD8^+$ T cell infiltration after treatment with (I) Control, (II) Gel, (III) Gel@GM-CSF, (IV) Gel@RSL3, (V) Gel@RSL3+GM-CSF and (VI) Gel@RSL3+GM-CSF-aPD-L1. * indicates significance at $P < 0.05$, ** indicates significance at $P < 0.01$, *** indicates significance at $P < 0.001$, **** indicates significance at $P < 0.001$.

Gel@RSL3+GM-CSF+aPD-L1 induced the most pronounced inhibition on both the primary and secondary tumors and the highest survival rate among all groups (Figs. 7b and S26). Interestingly, we observed that the extracted distal tumor tissues showed a modest decrease in cellular GPX4 activity that could be explained by the treatment-enhanced serum IFN-$\gamma$ levels, while the increase in MDA was negligible, suggesting that ferroptosis was not the primary contributor to the pronounced inhibition of the distal tumors thereof (Fig. S27). Meanwhile, we have observed many pro-immune alterations in the immune microenvironment of tumor tissues and lymph nodes (LNs). Specifically,

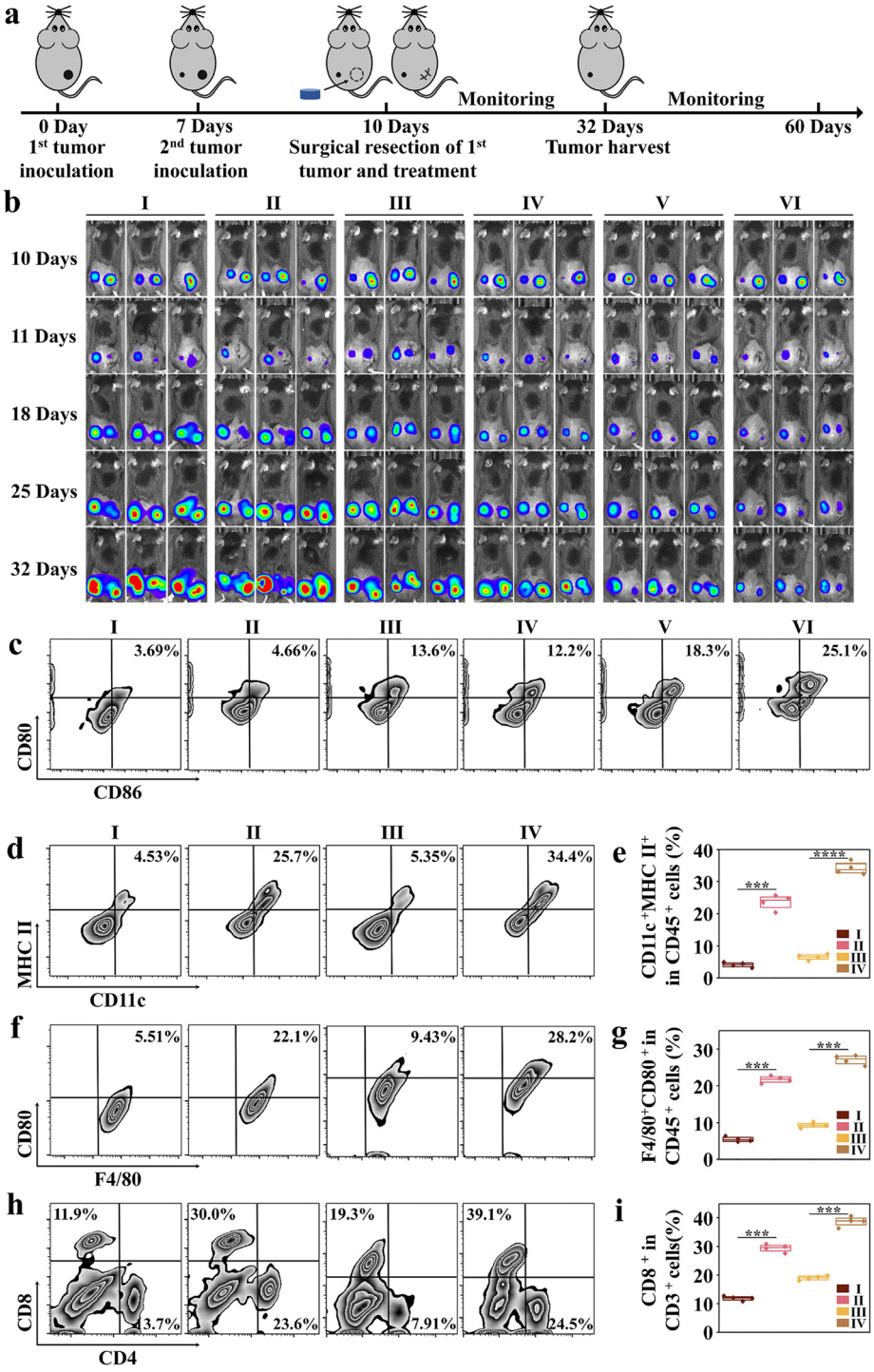


**Fig. 7. The biomimetic hydrogel stimulates systemic antitumor immune response to suppress distal tumors.** (a) Schematic illustration for establishing the bilateral tumor model and treatment schedule (n = 7). (b) In vivo bioluminescence images of B16F10-luc tumor-bearing mice throughout the treatment period with (I) Control, (II) Gel, (III) Gel@GM-CSF, (IV) Gel@RSL3, (V) Gel@RSL3+GM-CSF and (VI) Gel@RSL3+GM-CSF-aPD-L1. (c) Flow cytometric analysis on the DC maturation status in tumor-draining lymph nodes after treatment with(I) Control, (II) Gel, (III) Gel@GM-CSF, (IV) Gel@RSL3, (V) Gel@RSL3+GM-CSF and (VI) Gel@RSL3+GM-CSF-aPD-L1. (d-e) Flow cytometric analysis images (d) and quantification results (e) regarding the activation status of DCs ($CD11c^+/MHC\ II^+$) in primary and secondary tumors. I: Distal tumors in the untreated group. II: Distal tumors in the hydrogel-treated group. III: Primary tumors in the untreated group. IV: Primary tumors in the hydrogel-treated group (n = 4). (f-g) Flow cytometric analysis images (f) and quantification results (g) regarding the activation status of M1 macrophages ($F4/80^+/CD80^+$) in primary and secondary tumors (n = 4). I: Distal tumors in the untreated group. II: Distal tumors in the hydrogel-treated group. III: Primary tumors in the untreated group. IV: Primary tumors in the hydrogel-treated group. (h-i) Flow cytometric analysis (h) and quantification results (i) regarding the activation status of T cells ($CD4^+/CD8^+$) in different groups in primary and secondary tumors (n = 4). I: Distal tumors in the untreated group. II: Distal tumors in the hydrogel-treated group. III: Primary tumors in the untreated group. IV: Primary tumors in the hydrogel-treated group. *** indicates significance at $P < 0.001$, **** indicates significance at $P < 0.001$.

the treatment with Gel@RSL3+GM-CSF+aPD-L1 hydrogel triggered the highest DC maturation levels in tumor-draining LNs that was 6.8-fold higher than the control group (Fig. 7c). Flow cytometric analysis on the extracted tumor samples showed that the numbers of infiltrating M1 macrophages and mature DCs in the primary and distal B16F10 tumors of the Gel@RSL3+GM-CSF+aPD-L1 group have both increased significantly (Figs. 7d-g and S28a-d). In line with the critical roles of tumor-infiltrating mature APCs for the activation and recruitment of cytotoxic T cells, we found that the implanted Gel@RSL3+GM-CSF+aPD-L1 hydrogel induced the highest cytotoxic $CD8^+$ T cell infiltration in the primary and distal B16F10 tumors (Figs. 7h-i and S28e-f). These observations evidently suggested that the hydrogel implanted in the primary tumors stimulated potent systemic antitumor immunity and efficiently eliminated distal tumors, suggesting its potential application for the postoperative care of solid tumors to prevent recurrence.

## 4. Conclusion

In this work, we report an injectable hydrogel that could orchestrate potent local and systemic adaptive antitumor immunity to inhibit tumor recurrence post-resection. Immunotherapy for solid tumors has thus far been challenging due to the immunosuppressive microenvironment, insufficient immune cell infiltration and heterogenous, and their translation for resected tumors is more difficult due to the surgical stress-induced impairment of local immune system. By exploiting the immunogenic nature of the recently discovered ferroptosis cell death mode, the hydrogel locally delivered RSL3 to the microscopic tumor foci in the postoperative wound bed to trigger the release of tumor-associated DAMPs while also releasing GM-CSF to promote the in-situ maturation of APCs, thus creating an immunostimulatory tissue microenvironment to enable sustainable activation and recruitment of tumor-specific effector T cells. The significant expansion of activated cytotoxic T cells further exerts potent systemic antitumor effect for eliminating distal tumors. The enhanced IFN-$\gamma$ secretion by the activated T cells may also disrupt the redox balance of tumor cells via IFN-$\gamma$-SLC7A11-GSH-GPX4 axis to amplify the ferroptotic damage. Additionally, the hydrogel-encapsulated aPD-L1 could be gradually released during the treatment course to prevent premature T cell exhaustion by the IFN-$\gamma$-upregulated PD-L1 expression in tumor cells, substantially enhancing the robustness and persistence of the hydrogel-induced adaptive antitumor responses for sustainable protection.

Postoperative adjuvant therapy via localized delivery of chemotherapeutic drugs or radiosensitizing implants is a commonly applied technology in the clinics to inhibit tumor recurrence while limiting their potential systemic toxicities. However, the post-resection cavity usually presents complex topology that limits the accessibility of these therapeutic modality to the microscopic tumor foci. To address these clinical challenges, the molecularly engineered HA-based precursors could be solubilized in water and syringe-delivered to the resected cavity with high controllability for in-situ gelation, ensuring spread-filling of the resected tissue surface for maximum coverage of the residual microscopic tumors. Moreover, taking advantage of the NCSN-mediated reduction of quinone to catechol groups in dopamine units, the biomimetic hydrogel demonstrated high bioadhesiveness that may stably adhere to the resected site for sustained treatment and enhanced wound healing.

In the context of the immunotherapeutic activity of the biomimetic hydrogel, the HA precursors in the present study were individually modified with $\beta$-CD and PBA moieties for the hierarchical integration of the therapeutic components. Specifically, $\beta$-CD rings could trap hydrophobic RSL3 via host-guest inclusion, while PBA may form boronic ester bond with the hydroxyl groups in the glycosylated GM-CSF. Notably, the two interaction modes were intrinsically reversible that potentiated efficient local drug release after the HAase-mediated degradation of the HA scaffold, which is critical for preventing systemic ferroptosis toxicity. Meanwhile, the thiourea-catechol crosslinking and the intercalation of $\beta$-CD would generate a highly interconnected porous network with large pore sizes that could be used to trap macromolecular aPD-L1 species. In addition to regulating the drug delivery to achieve the immunostimulatory function, the hydrogel assembly protocol also avoids additional chemical modification on individual therapeutic components that preserves their natural bioactivity while eliminating potential safety concerns. These features above collectively highlight the clinically favorable advantages of the biomimetic hydrogels for postoperative treatment.

In summary, we have developed an injectable immunostimulant hydrogel as a biomimetic wound dressing for adjuvant immunotherapy of resected tumors. The molecularly engineered HA-CD-DA and HA-NCSN-PBA precursors could efficiently trap RSL3 and glycosylated GM-CSF in a reversible and non-invasive manner. The drug-loaded HA precursors are procedurally mixed with aPD-L1 and syringe-delivered to the resected cavity, and hydrogels are formed almost instantaneously upon adding a small dose of $NaIO_4$ oxidant to trigger rapid thiourea-catechol coupling. The biomimetic hydrogel may release RSL3 and GM-CSF into the resection margin inhibit microscopic residual tumors via cooperative ferroptosis-immunotherapy as well as elicit potent systemic antitumor immunity to eliminate distal tumors, while the concurrently released aPD-L1 could further ameliorate the negative impact of IFN-$\gamma$-upregulated PD-L1 expression on the robustness of adaptive antitumor immune responses. The immunotherapeutic hydrogel successfully overcame the insufficient APC maturation, impaired antigen cross-presentation and IFN-$\gamma$-mediated PD-L1 upregulation in the postoperative tumor bed and significantly prolonged mouse survival in both B16F10 and 4T1 tumor models, which may thus be a promising technology for the treatment of resected solid tumors in a broad spectrum of clinical scenarios.

## Declaration of competing interest

The authors declare that they have no conflicts of interest in this work.

## Acknowledgments

This work is supported by National Natural Science Foundation of China (32122048, 11832008, 92059107 and 51825302), Fundamental Research Funds for the Central Universities (2021CDJLXB001, 2020CDJ-LHZZ-037, 2021CDJZYJH-002 and 2020CDJYGZL009), Chongqing Outstanding Young Talent Supporting Program (cstc2021ycjh-bgzxm0124), Returning Overseas Scholar Innovation Program (CX2018062, CX2021098 and CX2020045), Natural Science Foundation of Chongqing Municipal Government (cstc2020jcyj-msxmX0834 and cstc2021jcyj-jqX0022).

## Supplementary materials

Supplementary material associated with this article can be found, in the online version, at doi:10.1016/j.fmre.2023.02.029.

## References

[1] A.G. Waks, E.P. Winer, Breast cancer treatment a review, JAMA 321 (3) (2019) 288–300.
[2] M. Banks, D. Graham, M. Jansen, et al., British Society of Gastroenterology guidelines on the diagnosis and management of patients at risk of gastric adenocarcinoma, Gut 68 (9) (2019) 1545–1575.
[3] F. Tang, Y. Tie, C. Tu, et al., Surgical trauma-induced immunosuppression in cancer: Recent advances and the potential therapies, Clin. Transl. Med. 10 (1) (2020) 199–223.
[4] J.G. Hiller, N.J. Perry, G. Poulogiannis, et al., Perioperative events influence cancer recurrence risk after surgery, Nat. Rev. Clin. Oncol. 15 (4) (2018) 205–218.
[5] A.N. Hosein, S.K. Dougan, A.J. Aguirre, et al., Translational advances in pancreatic ductal adenocarcinoma therapy, Nat. Cancer 3 (3) (2022) 272–286.
[6] P. Sargos, S. Chabaud, I. Latorzeff, et al., Adjuvant radiotherapy versus early salvage radiotherapy plus short-term androgen deprivation therapy in men with localised prostate cancer after radical prostatectomy (GETUG-AFU 17): A randomised, phase 3 trial, Lancet Oncol. 21 (10) (2020) 1341–1352.

[7] F. Zhou, J. Yang, Y. Zhang, et al., Local phototherapy synergizes with immunoadjuvant for treatment of pancreatic cancer through induced immunogenic tumor vaccine, Clin. Cancer Res. 24 (21) (2018) 5335–5346.
[8] Y. Lu, Q. Zhao, J.-Y. Liao, et al., Complement signals determine opposite effects of B cells in chemotherapy-induced immunity, Cell 180 (6) (2020) 1081–1097 e24.
[9] A.D. Waldman, J.M. Fritz, M.J. Lenardo, A guide to cancer immunotherapy: From T cell basic science to clinical practice, Nat. Rev. Immunol. 20 (11) (2020) 651–668.
[10] E.A. Stadtmauer, J.A. Fraietta, M.M. Davis, et al., CRISPR-engineered T cells in patients with refractory cancer, Science 367 (6481) (2020) eaba7365.
[11] X.J. Jiang, B.R. Stockwell, M. Conrad, Ferroptosis: Mechanisms, biology and role in disease, Nat. Rev. Mol. Cell Biol. 22 (4) (2021) 266–282.
[12] C. Mao, X. Liu, Y. Zhang, et al., DHODH-mediated ferroptosis defence is a targetable vulnerability in cancer, Nature 593 (7860) (2021) 586–590.
[13] D. Tang, X. Chen, R. Kang, et al., Ferroptosis: Molecular mechanisms and health implications, Cell Res. 31 (2) (2021) 107–125.
[14] X. Chen, R. Kang, G. Kroemer, et al., Broadening horizons: The role of ferroptosis in cancer, Nat. Rev. Clin. Oncol. 18 (5) (2021) 280–296.
[15] R. Song, T. Li, J. Ye, et al., Acidity-activatable dynamic nanoparticles boosting ferroptotic cell death for immunotherapy of cancer, Adv. Mater. 33 (31) (2021) 2101155.
[16] O. Kepp, G. Kroemer, Pro-ferroptotic fatty acid metabolism renders cancer cells immunogenic, Trends Cancer 8033 (22) (2022) 00089 -9.
[17] H. Liang, X. Wu, G. Zhao, et al., Renal clearable ultrasmall single-crystal Fe nanoparticles for highly selective and effective ferroptosis therapy and immunotherapy, J. Am. Chem. Soc. 143 (38) (2021) 15812–15823.
[18] W. Wang, M. Green, J.E. Choi, et al., CD8+ T cells regulate tumour ferroptosis during cancer immunotherapy, Nature 569 (7755) (2019) 270–274.
[19] X. Ma, L. Xiao, L. Liu, et al., CD36-mediated ferroptosis dampens intratumoral CD8+ T-cell effector function and impairs their antitumor ability, Cell Metab. 33 (5) (2021) 1001–1012 e5.
[20] P. Matzner, E. Sandbank, E. Neeman, et al., Harnessing cancer immunotherapy during the unexploited immediate perioperative period, Nat. Rev. Clin. Oncol. 17 (5) (2020) 313–326.
[21] Q. Chen, C. Wang, X. Zhang, et al., In situ sprayed bioresponsive immunotherapeutic gel for post-surgical cancer treatment, Nat. Nanotechnol. 14 (1) (2019) 89–97.
[22] Y. Chao, C. Liang, H. Tao, et al., Localized cocktail chemoimmunotherapy after in situ gelation to trigger robust systemic antitumor immune responses, Sci. Adv. 6 (10) (2020) eaaz4204.
[23] M. Mandai, J. Hamanishi, K. Abiko, et al., Dual faces of IFN$\gamma$ in cancer progression: A role of PD-L1 induction in the determination of pro- and antitumor immunity, Clin. Cancer Res. 22 (10) (2016) 2329–2334.
[24] J. Zhang, C. Chen, A. Li, et al., Immunostimulant hydrogel for the inhibition of malignant glioma relapse post-resection, Nat. Nanotechnol. 16 (5) (2021) 538–548.
[25] L. Scheetz, K.S. Park, Q. Li, et al., Engineering patient-specific cancer immunotherapies, Nat. Biomed. Eng 3 (10) (2019) 768–782.
[26] P. Patil, K.A. Russo, J.T. McCune, et al., Reactive oxygen species-degradable polythioketal urethane foam dressings to promote porcine skin wound repair, Sci. Transl. Med. 14 (641) (2022) eabm6586.
[27] Z. Álvarez, A.N. Kolberg-Edelbrock, I.R. Sasselli, et al., Bioactive scaffolds with enhanced supramolecular motion promote recovery from spinal cord injury, Science 374 (6569) (2021) 848–856.
[28] J.J. Green, J.H. Elisseeff, Mimicking biological functionality with polymers for biomedical applications, Nature 540 (7633) (2016) 386–394.
[29] D.-W. Zheng, W.-W. Deng, W.-F. Song, et al., Biomaterial-mediated modulation of oral microbiota synergizes with PD-1 blockade in mice with oral squamous cell carcinoma, Nat. Biomed. Eng. 6 (1) (2022) 32–43.
[30] X. Xu, X. Xia, K. Zhang, et al., Bioadhesive hydrogels demonstrating pH-independent and ultrafast gelation promote gastric ulcer healing in pigs, Sci. Transl. Med. 12 (558) (2020) eaba8014.
[31] S. Chan, N. Belmar, S. Ho, et al., An anti-PD-1–GITR-L bispecific agonist induces GITR clustering-mediated T cell activation for cancer immunotherapy, Nat. Cancer 3 (3) (2022) 337–354.
[32] J. Guo, H. De May, S. Franco, et al., Cancer vaccines from cryogenically silicified tumour cells functionalized with pathogen-associated molecular patterns, Nat. Biomed. Eng. 6 (1) (2022) 19–31.
[33] C. Liu, X. Liu, X. Xiang, et al., A nanovaccine for antigen self-presentation and immunosuppression reversal as a personalized cancer immunotherapy strategy, Nat. Nanotechnol. 17 (5) (2022) 531–540.
[34] Y. Liang, J. He, B. Guo, Functional hydrogels as wound dressing to enhance wound healing, ACS Nano 15 (8) (2021) 12687–12722.
[35] J. Zhang, Y. Zheng, J. Lee, et al., A pulsatile release platform based on photo-induced imine-crosslinking hydrogel promotes scarless wound healing, Nat. Commun. 12 (1) (2021) 1670.
[36] B. Guo, R. Dong, Y. Liang, et al., Haemostatic materials for wound healing applications, Nat. Rev. Chem. 5 (11) (2021) 773–791.
[37] Y.J. Xu, K. Wei, P. Zhao, et al., Preserving the adhesion of catechol-conjugated hydrogels by thiourea–quinone coupling, Biomater. Sci. 4 (12) (2016) 1726–1730.
[38] W. Zhang, R. Wang, Z. Sun, et al., Catechol-functionalized hydrogels: Biomimetic design, adhesion mechanism, and biomedical applications, Chem. Soc. Rev. 49 (2) (2020) 433–464.
[39] E.E. Leonhardt, N. Kang, M.A. Hamad, et al., Absorbable hemostatic hydrogels comprising composites of sacrificial templates and honeycomb-like nanofibrous mats of chitosan, Nat. Commun. 10 (1) (2019) 2307.
[40] M.K. Park, M.-X. Li, I. Yeo, et al., Balanced adhesion and cohesion of chitosan matrices by conjugation and oxidation of catechol for high-performance surgical adhesives, Carbohydr. Polym. 248 (2020) 116760.
[41] C.G. Park, C.A. Hartl, D. Schmid, et al., Extended release of perioperative immunotherapy prevents tumor recurrence and eliminates metastases, Sci. Transl. Med. 10 (2018) 433.
[42] Y. Xie, W. Hou, X. Song, et al., Ferroptosis: Process and function, Cell Death Differ. 23 (2016) 369.
[43] D. Tang, O. Kepp, G. Kroemer, Ferroptosis becomes immunogenic: Implications for anticancer treatments, Oncoimmunology 10 (1) (2020) 1862949 -1862949.
[44] H. Phuengkham, C. Song, S.H. Um, et al., Implantable synthetic immune niche for spatiotemporal modulation of tumor-derived immunosuppression and systemic antitumor immunity: Postoperative immunotherapy, Adv. Mater. 30 (18) (2018) e1706719.
[45] O. Bakos, C. Lawson, S. Rouleau, et al., Combining surgery and immunotherapy: Turning an immunosuppressive effect into a therapeutic opportunity, J. Immunother. Cancer 6 (1) (2018) 86.
[46] M. Shang, H. Yang, R. Yang, et al., The folate cycle enzyme MTHFD2 induces cancer immune evasion through PD-L1 up-regulation, Nat. Commun. 12 (1) (2021) 1940.

## Author profile

**Zhong Luo** obtained his B.Sc. degree from Chongqing University of Posts and Telecommunications in 2006 and his Ph.D. degree from Chongqing University in 2011. He then joined Prof. Yanli Zhao's group at Nanyang Technological University, Singapore, as a postdoctoral fellow and completed his training in 2015. Currently, he is a professor in the School of Life Science, Chongqing University. His research interests are focused on the design and development of innovative ferroptosis-dependent drug delivery nanosystems, aiming at new breakthroughs in vital fields including ferroptosis-based tumor therapy, suppression of innate ferroptosis defense, and immune-ferroptosis interactions.